THE PREDICTION OF PRESSURE DISTRIBUTIONS ON AN ARROW-WING CONFIGURATION INCLUDING THE EFFECT OF CAMBER, TWIST, AND A WING FIN*

Marjorie E. Manro
Boeing Commercial Airplane Company

Percy J. Bobbitt
NASA Langley Research Center

Robert M. Kulfan
Boeing Commercial Airplane Company

SUMMARY

Wind-tunnel tests of an arrow-wing body configuration consisting of flat, twisted, and cambered-twisted wings have been conducted at Mach numbers from 0.40 to 2.50 to provide an experimental data base for comparison with theoretical methods. A variety of leading- and trailing-edge control-surface deflections were included in these tests, and in addition, the cambered-twisted wing was tested with an outboard vertical fin to determine its effect on wing and control-surface loads. Theory-to-experiment comparisons of detailed pressure distributions have been made using current state-of-the-art attached-flow methods, as well as newly developed attached- and separated-flow methods. The purpose of these comparisons was to delineate conditions under which these theories can provide accurate basic and incremental aeroelastic loads predictions. Special emphasis is given to a new procedure developed by Robert Kulfan which shows promise of being able to predict the onset of a leading-edge vortex on thick and/or warped wings. Knowledge of the onset and position of vortices could be most valuable in conjunction with separated-flow methods to predict pressure distributions.

Theory-experiment comparisons show that current state-of-the-art linear and nonlinear attached-flow methods were adequate at small angles of attack typical of cruise conditions. The incremental effects of outboard fin, wing twist, and wing camber are most accurately predicted by the advanced-panel method PANAIR. Results of the advanced-panel separated-flow method, obtained with an early version of the program, show promise that accurate detailed pressure predictions may soon be possible for an aeroelastically deformed wing at high angles of attack.

---

*This work was performed under contracts NAS1-12875, NAS1-14141, NAS1-14962, and NAS1-15678 for the NASA Langley Research Center; and supplemented by the Boeing Commercial Airplane Company Independent Research and Development Program.

INTRODUCTION

A program has been under way for the past five years to examine the ability of state-of-the-art and advanced theoretical methods to predict aeroelastic loads on highly swept wings. A parallel objective has been to obtain an experimental data base of the type best suited for such a task. Three wing models were chosen for the test program; all had the same planform and airfoil section but one was flat, one twisted, and one had both camber and twist. With this combination, the incremental effects of twist, camber, and camber-twist, as predicted by theory, could be correlated with experiment. Other geometric variables included in the program are wing leading-edge radius, leading- and trailing-edge control-surface deflections, and an outboard fin. Most of the data obtained has been at subsonic and transonic speeds in the Boeing Transonic Wind Tunnel; however, the flat and twisted wings were also tested in the 9 by 7-foot supersonic portion of the Ames Unitary Wind Tunnel in order to fully examine existing and newly formulated panel methods, which apply for both subsonic and supersonic flows.

The present paper will concentrate mainly on the data obtained in recent wind-tunnel tests of the cambered-twisted wing and some new developments in separated-vortex methods and an attached-flow advanced-panel method. With the aid of the newly acquired data the incremental effects of twist, twist and camber, control-surface deflection, and outboard fin on wing pressure distributions may be illustrated. The improved separated-flow methodology permits some new insights into the conditions necessary for the formation of, and the prediction of the point of origin of, a leading-edge vortex.

Results of the subsonic-transonic program for the flat and twisted wings are summarized in NASA SP-347 (ref. 1) and discussed in more detail in references 2 through 5. The supersonic data for these two wings are available in references 6 through 8.

PANAIR advanced-panel attached-flow method calculations used in this paper were obtained with the assistance of James L. Thomas of the NASA Langley Research Center and Forrester Johnson and Edward Tinoco of the Boeing Military Airplane Company.

SYMBOLS AND ABBREVIATIONS

BL	buttock line, cm
b	wingspan, cm
$C_{L,V}$	vortex lift coefficient increment
C_M	pitching moment coefficient (moments about $0.25\bar{c}$)
C_N	normal force coefficient
C_n	section normal force coefficient
C_p	surface pressure coefficient

$C_{p,net}$	lifting pressure coefficient
C_s	suction force coefficient
c	local chord length, cm
$\bar{c}$	mean aerodynamic chord, cm
c_r	root chord, cm
L.E.	leading edge
M	Mach number
MS	model station, cm
T.E.	trailing edge
x,y,z	orthogonal coordinates
WRP	wing reference plane
α	angle of attack, deg
$\delta_{T.E.}$	trailing-edge control-surface deflection, deg
ϕ	velocity potential, cm/sec

MODELS

The wind-tunnel-model configuration selected for this study is a highly-swept (71.2°) thin wing (3.36-percent maximum thickness) of aspect ratio 1.65, mounted on the bottom of a slender body. The planform and basic geometry of the model are shown in figure 1. Three complete wings were constructed: one with no camber or twist, one with no camber but a spanwise twist variation (fig. 1), and one with both camber and twist. The twist of this third wing was the same as the plain twisted wing. The camber is a combination of a typical cruise airfoil camber and an estimate of the aeroelastic deformation at a moderate positive angle of attack. The resulting camber at the tip is approximately a 6° arc of a circle with the leading and trailing edges up. Sections at the root, mid-span, and tip (fig. 2) show not only the camber but the position of the sections of the cambered-twisted wing and the twisted wing, relative to the wing reference plane (flat wing).

All wings were designed to permit deflection of either partial- or full-span, 25-percent chord, trailing-edge control surfaces, with brackets, to allow streamwise deflections of $\pm 4.1^\circ$, $\pm 8.3^\circ$, $\pm 17.7^\circ$, and $\pm 30.2^\circ$, as well as 0°. In addition, the flat wing was provided with removable leading-edge segments that extended over 15 percent of the streamwise chord. These segments permitted testing of the leading edge drooped 5.1° and 12.8°, as well as undeflected. To

examine the effects of leading-edge shape, a segment with a sharp leading edge was constructed for the flat wing. Figure 1 shows the basic rounded leading edge with the sharp leading edge superimposed. A streamwise fin located at 72.5-percent semispan was provided for the cambered-twisted wing. The apex of the 71.2° sweep fin was located at 15-percent local chord of the wing (fig. 1) and has a 3-percent biconvex airfoil section.

The capability to measure the detailed load distribution on the wing and body of this configuration was provided by distributing 300 pressure orifices on the model. Each wing had 217 pressure orifices, equally divided into 7 streamwise sections on the left half. Pressure taps were located on both the top and bottom surfaces at the chordwise locations shown in figure 3. Pressure orifices we · located on the body in 5 streamwise rows of 15 orifices each. An additional 8 orifices in the area of the wing-body junction made a total of 83 orifices on the left side of the body.

To ensure close control of the model dimensions, a computerized lofting program was used to provide data for machining the model components using numerically controlled operations. The model was constructed of steel to minimize aeroelastic deflections.

WIND-TUNNEL TESTS

The model was tested in the Boeing Transonic Wind Tunnel (BTWT) and in the supersonic 9- by 7-foot leg of the NASA Ames Unitary Wind Tunnel. The former is a continuous-flow, closed-circuit, atmospheric facility with a 12.5-percent porosity test section measuring 8 by 12 by 14.5 feet; the latter is a continuous-flow, closed-circuit, variable-density facility with a test section measuring 7 by 9 by 18 feet. Seven Mach numbers from 0.40 to 1.11 were tested in the BTWT, with angle of attack varying from -8° to +16°. In the Ames facility, data were obtained primarily at Mach numbers of 1.7, 2.1, and 2.5. The major configurations tested are shown in tables I and II. Photographs of the model installed in the test sections are shown in figures 4 through 7.

FLOW PHENOMENA

Before assessing the ability of theoretical methods to predict the experimental pressure distributions, it is useful to understand the characteristics of the experimental flow field. This can be facilitated by looking at some pressure distributions at Mach number 0.40 for the rounded-leading-edge flat wing shown in figures 8 and 9. It should be noted, in the figures of pressure distributions, that symbols were generally omitted for clarity. At 16° angle of attack, however, the symbols were included to show the density of the available experimental data. At the low angles of attack, the flow is still attached, except for the station nearest the tip at 4° angle of attack. The fact that the vortex has started to form is indicated by the reduction in the peak pressure in the chordwise pressure distribution (fig. 8), and by the closeness of the constant-pressure lines in the isobars (fig. 9). The vortex is well developed

on the outboard half of the wing at 8°, and by 10° the vortex flow is affecting the entire wing.

The development of the vortex is modified by the shape of the leading edge as can be seen by comparing figures 8 and 9 with figures 10 and 11, which are for the sharp-leading-edge flat wing. The vortex develops much more rapidly for the sharp-leading-edge wing and is established over most of the wing at 4° angle of attack. At the higher angles of attack the leading-edge shape seems to lose importance as the flow at 16° is quite similar for both the sharp and rounded leading edges.

The effect of aeroelastic deformation is of prime interest in this study. Aeroelastic deformation is idealized in this study as a combination of pure twist and incremental camber. The camber that was used on this model is a combination of cruise camber and an aeroelastic camber, calculated for an arrow-wing similar to the one used in this study. The models with twist and camber-twist are assumed to be aeroelastically deformed versions of the flat wing. On the wing with twist only (figs. 12 and 13), the vortex formation is delayed until 8° angle of attack and then develops rapidly. At 12° the vortex flow affects the entire wing just as on the flat wing. The twisted wing is washed out 4.5° at the tip so that the local angles of attack at the tip of the flat and twisted wings are similar when vortex flow starts. The available models do not have camber alone, so the effect seen in figures 14 and 15 is for the cambered-twisted wing. The camber is leading and trailing edges up, so that the local leading-edge angle of attack is more like the flat wing, even though the twist is the same as that of the twisted wing. The formation of the vortex flow indicates that the local leading-edge angle of attack is the controlling feature.

Another geometric feature of interest for current low-aspect-ratio configurations is a wing fin. Pressure distributions and isobars on the cambered-twisted wing with an outboard fin are shown in figures 16 and 17. The pressures seem little affected by the fin at 4° and 6° angle of attack, but at 8° the pressure just outboard of the fin indicates that the fin has reduced the influence of the vortex off the wing apex in this area. There is some indication, however, that a second vortex is forming off the apex of the fin. This blocking effect is even more pronounced at the higher angles. Inboard of the fin the pressures are very similar to those with the fin off except at the station closest to the fin. Clearly, the effect of a fin needs to be studied in more detail to assess the effect of position and cant angle as well as whether the same interference effects are obtained on wings with different camber or twist.

The trends shown here are typical of the higher Mach numbers as well.

THEORETICAL METHODS

Theoretical calculations carried out in this study for both attached and detached flows (table III) are based on potential-flow theories. Results from three attached-flow panel methods which satisfy the classical Prandtl-Glauert equation for linearized compressible flow are presented. The first method uses

the constant-pressure-panel formulation, is valid for both supersonic and subsonic analysis, and satisfies only planar boundary conditions. The second method is a lower order panel method (constant strength sources and doublets) which is limited to subsonic flow but can satisfy boundary conditions on the exact configuration surface. The third method is a higher order panel method using bi-quadratic doublet and bi-linear source panels, valid for both supersonic and subsonic flow, and capable of satisfying exact boundary conditions.

The separated-flow method is an extension of the third attached-flow theory, based on distributions of quadratically varying doublet and linearly varying source panels. Since this approach is still under development and only preliminary results are available, it must be considered an advanced rather than a state-of-the-art method. As the older separated-flow methods capable of giving detailed pressure distributions can handle only simple wing geometries (straight leading-edge deltas), theory-experiment comparisons for an arrow wing would be of limited usefulness.

One of the most successful methods for the prediction of forces and moments produced by wings with leading edge separation is the Polhamus suction analogy. R. M. Kulfan's recent extensions to this method, to account for the effects of wing thickness and warp on the development of the vortex, are outlined. Additional details of the analytical methods are discussed below.

Attached-Flow Theories

The primary analysis method used for pressure calculations in this study was the unified subsonic/supersonic panel technique of FLEXSTAB, which was developed by Boeing under NASA Ames sponsorship (ref. 9). The FLEXSTAB system of digital computer programs uses linear theory to evaluate the static and dynamic stability, the inertial and aerodynamic loading, and the resulting elastic deformations of aircraft configurations. The aerodynamic module contained in the FLEXSTAB system is based on the constant-pressure-panel method developed by Woodward (refs. 10 through 12) to solve the linearized potential-flow equations for supersonic and subsonic speeds with planar boundary conditions. The method can also produce answers for transonic speeds, although the nonlinear terms not accounted for become important as sonic speed is approached.

Figure 18 shows the distribution of panels used in this analysis. Line sources and doublets are distributed along the longitudinal axis of the body to simulate its thickness and lifting effects. Similarly, source and vortex panels are placed in the plane of the wing to simulate its thickness and lifting effects. To account for the interference effects between the wing and body, constant-pressure vortex panels are placed on a shell around the body. This "interference" shell serves to cancel the normal velocity components on the body that are induced by the wing.

At subsonic Mach numbers and the high supersonic Mach numbers, 50 line singularities, 168 interference panels, and 160 wing panels were used to represent the configuration. For the very low supersonic Mach numbers (1.05 and 1.11), the number of interference panels had to be greatly increased (to 330) to overcome instabilities associated with the solution. The edges of the wing

panels were chosen to coincide with the control-surface hinge lines and break lines. Note on figure 18 that the panels are of nearly equal width and, in the chordwise direction, panel edges are at constant percent chord with closer spacing at the leading edge and the hinge lines.

The second attached-flow method used was the general method of Rubbert and Saaris (refs. 13 through 15) for the numerical solution of nonplanar, three-dimensional boundary-value problems. The method solves the exact incompressible potential-flow equation (Laplace's equation), with compressibility effects incorporated via the Gothert rule. In contrast to FLEXSTAB, the Rubbert-Saaris solution (hereafter referred to as TEA-230) is not encumbered by the small perturbation approximation and is capable of treating problems of far more detail and generality than the linearized theories.

Figure 19 shows a typical paneling scheme used for the TEA-230 representation of the arrow-wing body model. The source panels are placed on the configuration surface; consequently, new paneling was required for each configuration. The linearly varying internal and trailing vortex panel networks are not shown.

The third and most recently developed attached-flow method is the higher-order panel method developed by Ehlers, Epton, Johnson, Magnus, and Rubbert (refs. 16 through 20) which uses bi-quadratic doublet and bi-linear source panels. This method, known as PANAIR (Panel Aerodynamics), is still under development; therefore, the current predictions were made using the pilot code. The method will solve a variety of boundary value problems in steady subsonic and supersonic inviscid flow. The solutions are governed by the classical Prandtl-Glauert equation for linearized compressible flow. Boundary conditions are satisfied on the configuration surface so that new paneling is required for each configuration. Figure 20 shows the paneling for the cambered-twisted wing with the fin attached. The wing was represented by 476 panels, the body by 232, and the fin by 60. In addition, wake networks shed from all trailing edges extend more than 56 meters behind the configuration, but for clarity are not shown.

Detached-Flow Theory

The method chosen to predict the effect on wing pressures of the leading-edge spiral vortex was that of Weber, Brune, Johnson, Lu, and Rubbert (refs. 21 through 27). This leading-edge vortex (LEV) method is capable of predicting forces, moments, and detailed surface pressures on thin wings of arbitrary planform. The wing geometry is arbitrary in the sense that leading and trailing edges may be swept, as well as curved or kinked, provided that a single vortex describes the flow and the origin can be specified. The method does not represent the secondary vortices that often form under the primary leading-edge vortex.

The governing equations are the linear flow differential equation and nonlinear boundary conditions, which require that the flow be parallel to the wing surface and that the free vortex sheet, springing from the leading and trailing edges, be aligned with the local flow and support no pressure jump.

The Kutta condition is imposed and satisfied along all wing edges. This problem is solved numerically by an aerodynamic panel method. The configuration is represented by quadilateral panels on all surfaces, with quadratically varying doublet singularities distributed on the panels. The vortex core is modeled as a simple line vortex that receives vorticity from the free sheet through a connecting kinematic sheet. The set of nonlinear equations is solved by an iterative procedure, starting with an assumed initial geometry.

The example calculations using this method were obtained with an early version of the program which handled only thin flat wings. Figure 21 shows the paneling arrangement used on the wing. Note that the leading and trailing edges are extended to a point, rather than chopped off to form a tip with a finite chord. This should have only a trivial effect on the answers obtained. The fuselage was not a part of the current model; instead, the wing external to the body was moved inboard to obtain a more realistic model of the wing alone. A total of 212 panels were used for this solution: 63 panels to describe the wing, 108 panels to describe the rolled-up vortex, and 41 panels to describe the wake. This version of the program was restricted to incompressible flow.

Although the separated-flow computer program described above is still in development, the capability for handling wing thickness, camber, and twist, as well as a fuselage representation, have recently been added. In addition, the effects of compressibility, and many improvements on the numerics in order to facilitate convergence of the solution, have been incorporated since this prediction was made.

Leading-Edge Suction Analogy

The Polhamus leading-edge suction analogy, first published in 1966 (ref. 28), was initially developed to predict lift and pitching moment on thin, sharp-leading-edge delta wings. Subsequent developments (refs. 29 through 35) have extended the method to more arbitrary thin wing planforms. The suction analogy does not predict pressure distributions, but has been shown to provide accurate estimates of lift and pitching moment for a wide range of thin sharp-leading-edge flat wing configurations. Because configurations of interest have pointed or rounded rather than sharp leading edges, have camber and twist, and also deform aeroelastically, the previously mentioned analogy does not apply as orginally formulated. R. M. Kulfan has developed extensions to the suction analogy which overcome these limitations (refs. 36 and 37). Kulfan has observed, as have many others, that wing thickness has a retarding effect on the growth of leading-edge vortices. The experimental results indicate that, because of thickness, the vortex forms at an angle of attack greater than zero degrees. The vortex then grows with reduced strength, relative to a very thin wing, at the same angles of attack. The retarding effect depends not only on the thickness distribution, but also on whether the airfoil nose is pointed or rounded.

The formation of the leading-edge vortex is associated with the very high negative pressure and subsequent steep adverse pressure gradient near the leading edge of a highly swept wing at an angle of attack. The steep adverse pressure gradient can readily cause the three-dimensional boundary layer to

separate. When separation occurs, the boundary layer leaves the wing surface along the leading edge and rolls up into a region of concentrated vorticity. This is the leading-edge vortex.

The basic features of the suction analogy are depicted in figure 22. The bottom left-hand side of the figure depicts the attached-flow situation where linear theory predicts a square root singularity in the pressure at the leading edge. This singularity in turn produces a suction force in the plane of the wing. In practice, the flow at moderate angles of attack becomes like that depicted on the right-hand panel of the wing in figure 22. The flow separates off the leading edge, a vortex forms above the wing, and the flow reattaches inboard of the leading edge. The suction analogy assumes that the force required to make the flow over the vortex attach on the upper surface is the same as the leading-edge suction force necessary to produce the attached-flow condition. For attached flow, the suction force acts in the chord plane of the wing. The suction force for vortex flow acts normal to the plane of the wing, producing vortex lift.

The leading-edge vortex springs uniformly from the full leading edge of thin sharp-edge flat wings. Pointed- and rounded-nose airfoils, however, reduce the adverse pressure near the leading edge of highly swept wings. This effect is greatest over the inboard portion of the wing. Leading-edge separation in this case starts near the wing tip and moves progressively inboard with increasing angle of attack.

The suction analogy, previously applied only to thin sharp-leading-edge wings, has been extended by Kulfan to account for the effects of wing airfoil shape and thickness on the progressive growth of leading-edge vortices on flat wings. The qualitative effects of pointed- and rounded-nose airfoil thickness on vortex lift can be understood by applying the suction analogy reasoning to these airfoils as shown in figure 23. On the pointed-nose airfoil, the flow forward of the lower surface dividing streamline has a smaller turn around the leading edge to the upper surface than on the thin sharp-leading-edge airfoil, and on the rounded-nose airfoil, a smaller, smoother turn. Hence, the net centrifugal force necessary to turn the attached flow is less than that required for a thin sharp-leading-edge wing. The assumption is now made that the pressure required to produce reattached vortex flow on the thick wing is again equal to that necessary to produce attached flows. This reduced force is called the effective suction force. The start of the vortex is delayed to a higher angle of attack for these leading edges. For the pointed nose, the angle at which vortex lift starts is related to the angle at which the upper surface attains a positive angle of attack. The vortex lift on the rounded nose airfoil starts when the suction coefficient becomes greater than the parabolic nose drag. The method to obtain the suction force and the resulting vortex lift is described in reference 36 and includes many comparisons to experimental data.

The elegance of the Polhamus suction analogy approach is that linear theory is used to successfully predict the nonlinear forces associated with leading-edge vortices. The nonlinearity in the suction analogy occurs because the leading-edge suction depends on $\sin^2\alpha$. An additional nonlinearity was introduced by the methods previously discussed, to account for the retarding effects

of pointed-nose and rounded-nose airfoils on the progressive development of the leading-edge vortex.

Since the essential element in this calculation is the linear theory calculation of the leading-edge suction, the method for predicting rounded-nose airfoil effects on vortex development can be extended readily to arbitrary highly-swept warped wings to account for the effects of camber, twist, control-surface deflections, or aeroelastic distortions. This extension is discussed in reference 37.

THEORY-TO-EXPERIMENT COMPARISONS

The usefulness of any aerodynamic theory is determined by its ability to accurately predict flight or wind-tunnel results. The predictive methods available as production tools, as well as newly developed methods, must be tested against experimental data for those configurations and flight conditions which will figure in the design analysis. With this in mind, and recognizing the limited amount of detailed pressure data available for arrow-wing configurations over the entire subsonic-supersonic speed regimes, the present experimental and associated theoretical-methods evaluation were undertaken.

Attached-Flow Methods

Theory-to-experiment comparisons were made over a range of Mach numbers from 0.40 to 2.50 using the FLEXSTAB system, at Mach numbers of 0.40 and 0.85 with the TEA-230 program, and at Mach numbers of 0.40, 0.85, and 1.05 using the PANAIR pilot code. All configurations (except the cambered-twisted wing with fin on), including deflected control surfaces, were analyzed with FLEXSTAB. The flat and twisted wings, including some deflected control-surfaces, were analyzed using TEA-230. The three wings without deflected control-surfaces, but including the effect of the wing fin, were analyzed using PANAIR. The comparisons discussed in this paper will be limited to configurations with the control surfaces undeflected, although experimental control surface data will be shown.

Initial trade studies in the process of designing aircraft are often limited to experimental force data only, if in fact any experimental data is available at this stage. Even with the availability of pressure data, force and moment data are required for performance and stability evaluations. Forces and moments presented in subsequent figures are obtained by integrating the pressure data. Figures 24 through 26 show comparisons of attached-flow method predictions of wing normal force and pitching moment coefficients to the experimental data for three Mach numbers. At low and moderate angles of attack the predictions are quite good. At the higher angles of attack, FLEXSTAB appears to be better than the other methods - TEA-230 and PANAIR both underpredict normal force - although as we have seen in figures 8 through 17 there is strong vortex flow at these angles and FLEXSTAB does not include this phenomena. This apparent agreement is fortuitous, and detailed comparisons of surface pressures are necessary to evaluate the adequacy of these theoretical solutions in describing the load distribution.

A good test of a theoretical tool is whether or not the pressure change due to a change in twist and/or camber can be accurately predicted. Figures 27 through 34 show comparisons of experimental data with results from the theoretical methods at an angle of attack of 0° and Mach numbers of 0.40 and 1.05. The predictions for the flat wing (figs. 27 and 28) are quite good for all theories, although PANAIR is definitely better at the leading edge at Mach 1.05. Figures 29 and 30 show the twisted wing where it is clear that PANAIR (and TEA-230 at Mach 0.40) is much better than FLEXSTAB. The cambered-twisted wing, fin off and on, are shown in figures 31 through 34. The predictions are again very good, except at the outboard station at Mach 1.05 where the pressures on the lower surface are overpredicted. It seems as if the change in pressures for this smooth continuous type of deformation are adequately predicted in the region where the flow is still attached.

Comparisons of experimental and theoretical surface pressure distributions at a Mach number of 0.40 and angle of attack of 4° are shown in figures 35 through 38 for the four configurations. The predictions of all methods shown seem quite good, PANAIR and TEA-230 being somewhat better than FLEXSTAB at the leading edge. Figures 39 through 42 show a similar comparison at 8° angle of attack. The comparison on the twisted wing is still quite good, although a vortex has started to form outboard of the last section shown. On the other wings the vortex is developed on the upper surface, so that the predictions are poor. The lower surface predictions, however, are still quite acceptable.

Comparisons at a Mach number of 1.05 and an angle of attack of 4° are shown in figures 43 through 46. Although the predictions are good inboard, there is vortex development outboard on all but the twisted wing (fig. 44). It is interesting to note the difference in the vortex position at the tip section between the fin-off and fin-on data (figs. 45 and 46). With the fin off, the vortex is at mid chord, whereas with the fin on the vortex is near the leading edge. As the vortex moves inboard with increasing angle of attack, the predictions at 8° (not shown) are not as good as at 4°.

As attached-flow theories are inadequate to predict the pressure distributions at moderate angles of attack, it is important to determine whether theory could be used to predict the aeroelastic increment, to use in combination with rigid experimental data. Figures 47 through 58 show the incremental distributions due to change in shape at angles of attack of 0° and 8° and Mach numbers of 0.40 and 1.05.

The data for figures 47 through 50 were obtained by subtracting the flat wing data from the twisted wing data at each combination of angle of attack and Mach number. For this increment at M = 0.40, all three attached-flow theories can be evaluated. At $\alpha = 0^{\circ}$ they all predict the increment very well. FLEXSTAB, being a linear theory, predicts the same increment at all angles of attack, which is not the case in the experimental data, even on the lower surface. PANAIR and TEA-230, with their exact on-the-surface boundary conditions, predict the lower surface pressure increments quite well at all angles of attack shown. The difference in the position of the vortex on the upper surface of the two wing shapes is apparent in the incremental experimental data; none of the attached-flow theories predict this.

The increment due to camber alone is obtained by subtracting the data for the twisted wing from that of the cambered-twisted wing. These data are shown in figures 51 through 54. FLEXSTAB and PANAIR predict the increment very well at $\alpha = 0^{\circ}$, as would be expected from examining figures 29 through 32 (data at $\alpha = 0^{\circ}$). At $\alpha = 8^{\circ}$, although the lower surface predictions are good, the shift in vortex position on the upper surface is not predicted.

Figures 55 through 58 are the combined camber-twist increment (subtracting flat wing data from cambered-twisted wing data). The predictions at $\alpha = 0^{\circ}$ are again good. The mid-span station at $\alpha = 8^{\circ}$ tends to look a little better for the combined increment than it did for either twist or camber alone. This is because the position of the vortex on both the flat and cambered-twisted wings is more nearly the same, while the position on the twisted wing is shifted.

In addition to the increments due to change in wing shape, the effect of adding a vertical fin to the cambered-twisted wing is shown in figures 59 through 64. Theoretical predictions of the pressures with the fin on are limited to the PANAIR method. These figures show only the three outboard pressure stations; there is no change in pressure on the inboard portion of the wing due to adding the fin, either experimentally or as shown by PANAIR. For the Mach number angle-of-attack combinations where the flow is still attached, PANAIR predicts the increment well. The fin, however, has a large effect on the position and strength of the vortex. It is evident from figure 61 ($M = 0.40$, $\alpha = 8^{\circ}$) and figure 63 ($M = 1.05, \alpha = 4^{\circ}$) that the vortex has started and that the predictions would no longer be useful at these or larger angles of attack.

It is evident that the attached-flow methods are no better at predicting incremental pressures due to aeroelastic deformation when the flow is separated than they are in predicting the absolute pressure level. The use of attached-flow methods is clearly restricted to conditions, or at least regions of the wing, where attached flow exists.

Detached-Flow Method

It is obvious that as a vortex forms at moderate angles of attack on this configuration, attached-flow theories deteriorate in their ability to predict detailed pressures. Unfortunately this type of flow may exist at various points in the flight envelope and must be assessed in structural design. The advanced-panel leading-edge vortex method previously described is being developed to provide this capability. Results of this new procedure are shown in figure 65. These data are for 12° angle of attack and include a typical FLEXSTAB prediction for comparison. The LEV results are surprisingly good, especially considering the absence of the body in the theoretical model. The level of the peak lifting pressure is generally overpredicted, which at the apex may be because the vortex is actually further from the surface than the theory predicts, and for the outboard wing because there is a secondary vortex. Predictions for the other wings, for which experimental data are available, are planned for the near future. These solutions will also examine the effect of including the body and wing thickness in the model.

Leading-Edge Suction Analogy

The Polhamus leading-edge-suction analogy, as expanded by Kulfan, still does not predict pressure distributions, but accounts for wing thickness and warp in predicting the region over which the vortex exists. The insert in figure 66 shows a typical plot of experimental net pressure coefficient as a function of angle of attack. The angle of attack at which the pressure coefficients deviate from a linear relationship is the start of vortex flow. In the composite plots in this figure, the linear part of the $C_{p,net}$ vs. α curve at each spanwise location (at x/c = 0.025) is shown by the open squares; the nonlinear, or separated portion, is shown by the filled-in squares. The start of vortex flow, as predicted by the Kulfan method, is indicated by the solid lines. Figure 66 also illustrates the effect of wing warp on the progressive development of the leading-edge vortex. For a sharp thin airfoil the vortex would start on the appropriate surface midway between the boundaries shown (at $\alpha = 0^{o}$ for the flat wing). Using the information provided by the Kulfan method to predict the vortex location, the LEV code can be executed with the vortex restricted to that location. This procedure will be tried in the near future. If one's interest is only inboard of the vortex, the attached-flow theories can be used to predict pressures quite well, although, as can be seen in figure 66, the LEV code also provides excellent agreement with the experimental data in this area.

EXPERIMENTAL EFFECTS OF CONTROL-SURFACE DEFLECTION AND FIN

Experimental data were obtained for a wide range of configurations (see table I). One particularly interesting aspect is the effect of full- and partial-span trailing-edge control-surface deflections. Figure 67 shows span-load distributions on the flat wing at Mach 0.40. At all three angles of attack shown, the effect on the inboard wing loads is almost all due to the deflection of the inboard portion of the control surface. On the outboard wing the incremental load is just as great, or greater, when only the inboard portion is deflected, as it is when only the outboard control surface is deflected. This effect is noticeably greater at 12^{o} angle of attack.

Similar data for the twisted wing are shown in figure 68. The increments are very similar, with only the total load level changing due to the locally lower angle of attack outboard and the resulting position of the vortex. Figures 69 and 70 show the effect of trailing-edge control surface deflection on the cambered-twisted wing with the fin off and fin on respectively. The incremental control-surface data for fin off are again very similar to the previous wings. Comparing the fin-on data (fig. 70) to the fin-off data (fig. 69) shows that although the increment for full-span deflection is much the same, the deflection of the outboard portion has a larger effect on the outboard wing with the fin on - both inboard and outboard of the fin (located at 2y/b = 0.725).

The effect of angle of attack on the spanload distribution for both fin off and fin on is shown in figures 71 through 74 for the four deflected trailing-edge control-surface configurations. Figure 71 is for the undeflected case. The spanwise loading at 4^{o} angle of attack is the same for both fin off and fin

on, as is the loading on the inboard 70 percent of the wing at 8°. At higher angles of attack, when the fin is off, the load on the outboard quarter of the wing remains the same as it was at 8°, while the load inboard increases. With the fin on, however, it is only directly inboard of the fin ($2y/b = 0.65$) that the load remains at the 8° angle of attack level. The load increases as angle of attack increases on the rest of the wing. Figures 72, 73, and 74, which are respectively outboard only, inboard only, and full-span control-surface deflection, illustrate this same phenomena. The placement and orientation of the fin clearly needs further study to obtain the maximum benefit in a control effectiveness sense.

Theoretical pressure predictions made for the configuration with deflected trailing edge are not shown here, but have been previously reported in detail (refs. 2 and 5). The pressures at the hinge line are typically overpredicted, especially by FLEXSTAB and to some degree by TEA-230. PANAIR has not been used on this configuration to predict pressures for the deflected trailing edge.

CONCLUDING REMARKS

The previous discussion has shown that the arrow-wing configuration of this study is dominated by leading-edge vortex flow at moderate and high angles of attack. Attached-flow methods are very good at low angles of attack typical of cruise conditions (load factor one). At critical structural and control design conditions, which involve large angles of attack and/or large control-surface deflections, the attached-flow theories are inadequate. Examination of the theoretical incremental load caused by a change in shape, shows that attached-flow theories can be used to provide an aeroelastic increment to the rigid experimental data only at small angles of attack.

The one example of a separated flow method indicates much better agreement with experiment than do the attached-flow theories. If attempts to use it in conjunction with the Kulfan method to predict the location of the vortex are successful, an investigation must be made into the possibilities of including the aeroelastic effects in this procedure. At this time, this seems to be the best hope for predicting the aeroelastic loads on highly-swept, low-aspect-ratio, flexible airplanes with the accuracy required.

REFERENCES

1. Manro, Marjorie E.; Tinoco, Edward N.; Bobbitt, Percy J.; and Rogers, John T.: Comparisons of Theoretical and Experimental Pressure Distributions on an Arrow-Wing Configuration at Transonic Speeds. Aerodynamic Analyses Requiring Advanced Computers - Part II, NASA SP-347, 1975, pp. 1141-1188.

2. Manro, Marjorie E.; Manning, Kenneth J. R.; Hallstaff, Thomas H.; and Rogers, John T.: Transonic Pressure Measurements and Comparison of Theory to Experiment for an Arrow-Wing Configuration - Summary Report. NASA CR-2610, 1976.

3. Manro, Marjorie E.; Manning, Kenneth J. R.; Hallstaff, Thomas H.; and Rogers, John T.: Transonic Pressure Measurements and Comparison of Theory to Experiment for an Arrow-Wing Configuration, Volume I: Experimental Data Report - Base Configuration and Effects of Wing Twist and Leading-Edge Configuration. NASA CR-132727, 1975.

4. Manro, Marjorie E.; Manning, Kenneth J. R.; Hallstaff, Thomas H.; and Rogers, John T.: Transonic Pressure Measurements and Comparison of Theory to Experiment for an Arrow-Wing Configuration, Volume II: Experimental Data Report - Effects of Control Surface Deflection. NASA CR-132728, 1975.

5. Manro, Marjorie E.; Manning, Kenneth J. R.; Hallstaff, Thomas H.; and Rogers, John T.: Transonic Pressure Measurements and Comparison of Theory to Experiment for an Arrow-Wing Configuration, Volume III: Data Report - Comparison of Attached Flow Theories to Experiment. NASA CR-132729, 1975.

6. Manro, Marjorie E.; Bobbitt, Percy J.; and Rogers, John T.: Comparisons of Theoretical and Experimental Pressure Distributions on an Arrow-Wing Configuration at Subsonic, Transonic and Supersonic Speeds. Prediction of Aerodynamic Loading, AGARD-CP-204, Feb. 1977, pp. 11-1 - 11-14.

7. Bobbitt, Percy J.; and Manro, Marjorie E.: Theoretical and Experimental Pressure Distributions for a 71.2° Swept Arrow-Wing Configuration at Subsonic, Transonic, and Supersonic Speeds. Proceedings of the SCAR Conference - Part I, NASA CP-001, 1977, pp. 85-122.

8. Manro, M. E.: Supersonic Pressure Measurements and Comparison of Theory to Experiment for an Arrow-Wing Configuration. NASA CR-145046, 1976.

9. Tinoco, E. N.; and Mercer, J. E.: FLEXSTAB - A Summary of the Functions and Capabilities of the NASA Flexible Airplane Analysis Computer System. NASA CR-2564, 1975.

10. Woodward, F. A.; Tinoco, E. N.; and Larsen, J. W.: Analysis and Design of Supersonic Wing-Body Combinations, Including Flow Properties in the Near Field, Part 1 - Theory and Application. NASA CR-73106, 1967.

11. Woodward, Frank A.: Analysis and Design of Wing-Body Combinations at Subsonic and Supersonic Speeds. J. Aircr., vol. 5, no. 6, Nov.-Dec. 1968, pp. 528-534.

12. Dusto, A. R., et al.: A Method for Predicting the Stability Characteristics of an Elastic Airplane, Volume 1,- FLEXSTAB Theoretical Description. NASA CR-114712, 1974.

13. Rubbert, P. E.; Saaris, G. R.; Scholey, M. B.; Standen, N. M.; and Wallace, R. E.: A General Method for Determining the Aerodynamic Characteristics of Fan-in-Wing Configurations. Vol. I - Theory and Application. USAAVLABS Tech. Rep. 67-61A, U.S. Army, Dec. 1967.

14. Rubbert, P. E.; and Saaris, G. R.: A General Three-Dimensional Potential-Flow Method Applied to V/STOL Aerodynamics. SAE J., vol. 77, September 1969.

15. Rubbert, P. E.; and Saaris, G. R.: Review and Evaluation of a Three-Dimensional Lifting Potential Flow Analysis Method for Arbitrary Configurations. AIAA Paper No. 72-188, 1972.

16. Ehlers, F. E.; Epton, M. A.; Johnson, F. T.; Magnus, A. E.; and Rubbert, P. E.: An Improved Higher Order Panel for Linearized Supersonic Flow. AIAA Paper No. 78-15, January 1978.

17. Moran, Jack; and Tinoco, E. N.: User's Manual - Subsonic/Supersonic Advanced Panel Pilot Code. NASA CR-152047, 1978.

18. Ehlers, F. Edward; Epton, Michael A.; Johnson. Forrester T.; Magnus, Alfred E.; and Rubbert, Paul E.:. A Higher Order Panel Method for Linearized Supersonic Flow. NASA CR-3062, 1979.

19. Johnson, Forrester T.; and Rubbert, Paul E.: Advanced Panel-Type Influence Coefficient Methods Applied to Subsonic Flows. AIAA Paper No. 75-50, January 1975.

20. Tinoco, E. N.; Johnson, F. T.; and Freeman, L. M.: The Application of a Higher Order Panel Method to Realistic Supersonic Configurations. AIAA Paper No. 79-274, January 1979.

21. Weber, James A.; Brune, Guenter W.; Johnson, Forrester T.; Lu, Paul; and Rubbert, Paul E.: A Three-Dimensional Solution of Flows Over Wings With Leading Edge Vortex Separation. Aerodynamic Analyses Requiring Advanced Computers - Part II, NASA SP-347, 1975, pp. 1013-1032.

22. Brune, G. W.; Weber, J. A.; Johnson, F. T.; Lu, P.; and Rubbert, P. E.: A Three-Dimensional Solution of Flows Over Wings With Leading-Edge Vortex Separation. Part 1 - Engineering Document. NASA CR-132709, 1975.

23. Brune, G. W.; and Rubbert, P. E.: Boundary Value Problems of Configurations With Compressible Free Vortex Flow. AIAA Journal, vol. 15, no. 10, October 1977, pp. 1521-1523.

24. Gloss, Blair B.; and Johnson, Forrester, T.: Development of an Aerodynamic Theory Capable of Predicting Surface Loads on Slender Wings With Vortex Flow. Proceedings of the SCAR Conference - Part I, NASA CP-001, 1977, pp. 55-67.

25. Johnson, F. T.; Tinoco, E. N.; Lu, P.; and Epton, M. A.: Recent Advances in the Solution of Three-Dimensional Flow over Wings with Leading Edge Vortex Separation. AIAA Paper 79-282, January 1979.

26. Johnson, F. T.; Lu, P.; Tinoco, E. N.; and Epton, M. A.: An Improved Panel Method For the Solution of Three-Dimensional Leading-Edge Vortex Flows, Volume I, Theory Document. NASA CR-159173, 1980.

27. Tinoco, E. N.; Lu, P.; and Johnson, F. T.: An Improved Panel Method For the Solution of Three-Dimensional Leading-Edge Vortex Flows, Volume II, Users Guide and Programmers Document. NASA CR-159174, 1980.

28. Polhamus, Edward C.: A Concept of the Vortex Lift of Sharp-Edge Delta Wings Based on a Leading-Edge-Suction Analogy. NASA TN D-3767, 1966.

29. Polhamus, Edward C.: Application of the Leading-Edge-Suction Analogy of Vortex Lift to the Drag Due to Lift of Sharp-Edge Delta Wings. NASA TN D-4739, 1968.

30. Polhamus, Edward C.: Predictions of Vortex-Lift Characteristics by a Leading-Edge Suction Analogy. J. Aircr., vol. 8, no. 4, Apr. 1971, pp. 193-199.

31. Snyder, Melvin H., Jr.; and Lamar, John E.: Application of the Leading-Edge-Suction Analogy to Prediction of Longitudinal Load Distribution and Pitching Moments for Sharp-Edged Delta Wings. NASA TN D-6994, 1972.

32. Lamar, John E.: Extension of Leading-Edge-Suction Analogy to Wings With Separated Flow Around the Side Edges at Subsonic Speeds. NASA TR R-428, 1974.

33. Lamar, John E.: Some Recent Applications of the Suction Analogy to Vortex-Lift Estimates. Aerodynamic Analyses Requiring Advanced Computers - Part II, NASA SP-347, 1975, pp. 985-1011.

34. Lamar, J. E.: Subsonic Vortex-Flow Design Study for Slender Wings. AIAA Paper 78-154, January 1978.

35. Lamar, J. E.: Strake-Wing Analysis and Design. AIAA Paper 78-1201, July 1978.

36. Kulfan, R. M.: Wing Airfoil Shape Effects on the Development of Leading-Edge Vortices. AIAA Paper No. 79-1675, August 1979.

37. Kulfan, R. M.: Wing Geometry Effects on Leading-Edge Vortices. AIAA Paper No. 79-1872, August 1979.

TABLE I.- SUMMARY OF CONDITIONS TESTED IN THE BOEING TRANSONIC WIND TUNNEL

WING	TRAILING EDGE	LEADING-EDGE DEFLECTION, DEGREES	TRAILING-EDGE DEFLECTION, DEGREES
ROUNDED-LEADING-EDGE FLAT WING	FLAT	0.	0., ± 4.1, ± 8.3, ± 17.7, ± 30.2
			PARTIAL SPAN + 8.3, + 17.7
		PARTIAL SPAN 5.1	PARTIAL SPAN ± 8.3, ± 17.7
		5.1, 12.8	0., + 4.1, ± 8.3, ± 17.7
	TWISTED	0.	0., + 4.1, ± 8.3, ± 17.7
SHARP-LEADING-EDGE FLAT WING	FLAT	0.	0.
ROUNDED-LEADING-EDGE TWISTED WING	TWISTED	0.	0., + 4.1, ± 8.3, ± 17.7, + 30.2
			PARTIAL SPAN + 8.3
ROUNDED-LEADING-EDGE CAMBERED-TWISTED WING (VERTICAL FIN OFF AND ON)	CAMBERED-TWISTED	0.	0., + 8.3
			PARTIAL SPAN + 8.3

MACH NUMBERS: 0.40, 0.70, 0.85, 0.95, 1.00, 1.05, 1.11
ANGLE OF ATTACK: -8° TO + 16° (2° INCREMENTS)

TABLE II.- SUMMARY OF CONDITIONS TESTED IN THE NASA AMES UNITARY WIND TUNNEL

WING	TRAILING EDGE	LEADING EDGE DEFLECTION, DEGREES	TRAILING-EDGE DEFLECTION, DEGREES
ROUNDED-LEADING-EDGE FLAT WING	FLAT	0.	0., ± 4.1, +8.3
			PARTIAL SPAN +4.1, +8.3
		5.1	0.
SHARP-LEADING-EDGE FLAT WING	FLAT	0.	0.
		5.1	0.
ROUNDED-LEADING-EDGE TWISTED WING	TWISTED	0.	0., + 8.3

MACH NUMBERS: 1.70, 2.10, 2.50
ANGLE OF ATTACK: -8° TO + 14° (2° INCREMENTS) + 15°

TABLE III.- THEORETICAL PANEL METHODS

$$(\beta^2 \phi_{xx} + \phi_{yy} + \phi_{zz} = 0 \quad \beta^2 = 1 - M_\infty{}^2)$$

METHOD	BOUNDARY CONDITIONS	COMMENTS
FLEXSTAB	LINEARIZED	
TEA-230	'EXACT' ON THE SURFACE	
PAN AIR	'EXACT' ON THE SURFACE	
LEADING-EDGE VORTEX (LEV)	'EXACT' ON THE SURFACE SATISFIES BOTH NONLINEAR $\Delta C_p = 0$ AND STREAM SURFACE CONDITIONS	ITERATIVE SOLUTION

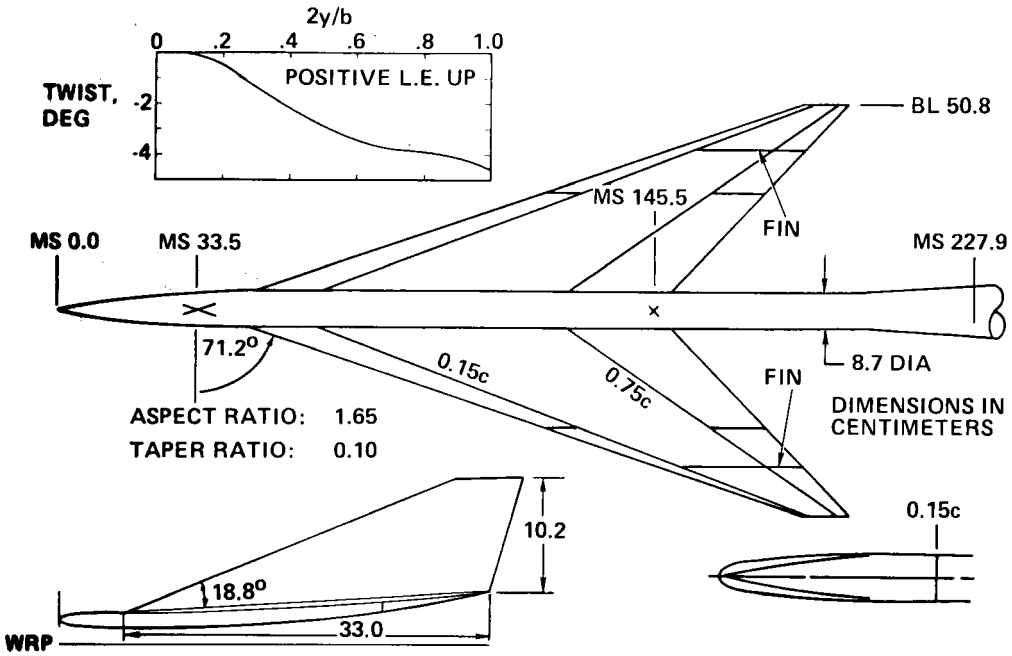

Figure 1.- General arrangement and characteristics.

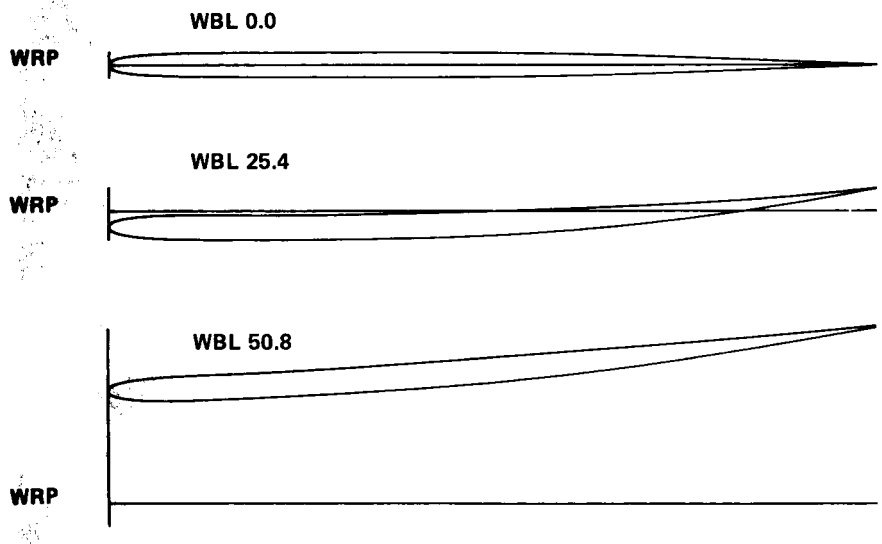

Figure 2.- Cambered-twisted wing section geometry.

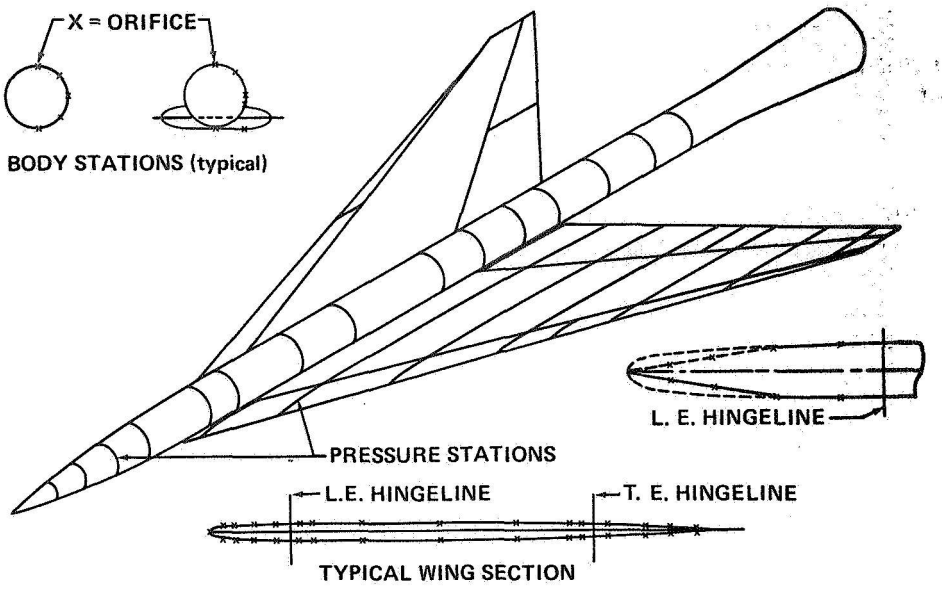

Figure 3.- Pressure orifice locations.

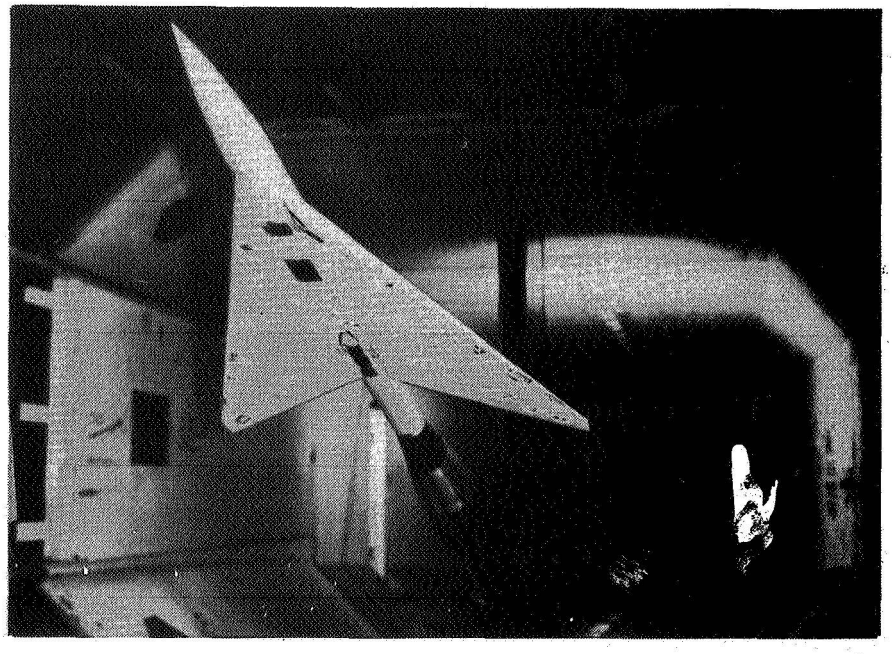

Figure 4.- Flat wing in Boeing Transonic Wind Tunnel.

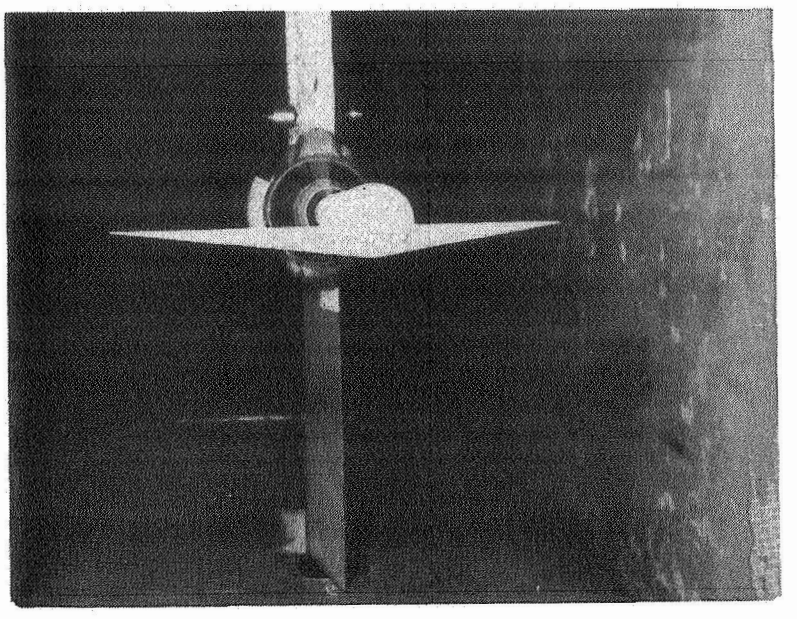

(a) Flat wing.

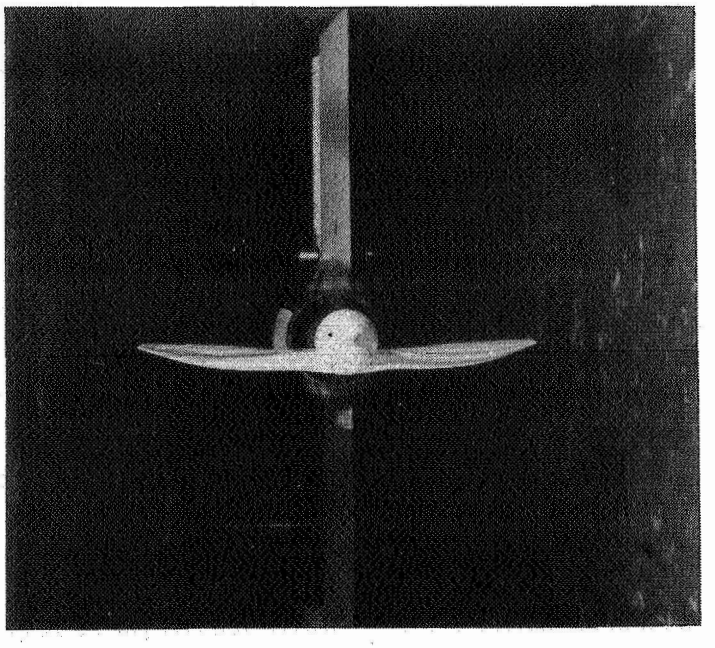

(b) Twisted wing.

Figure 5.- Flat and twisted wings in the 9- by 7-foot leg of the Ames Unitary Wind Tunnel.

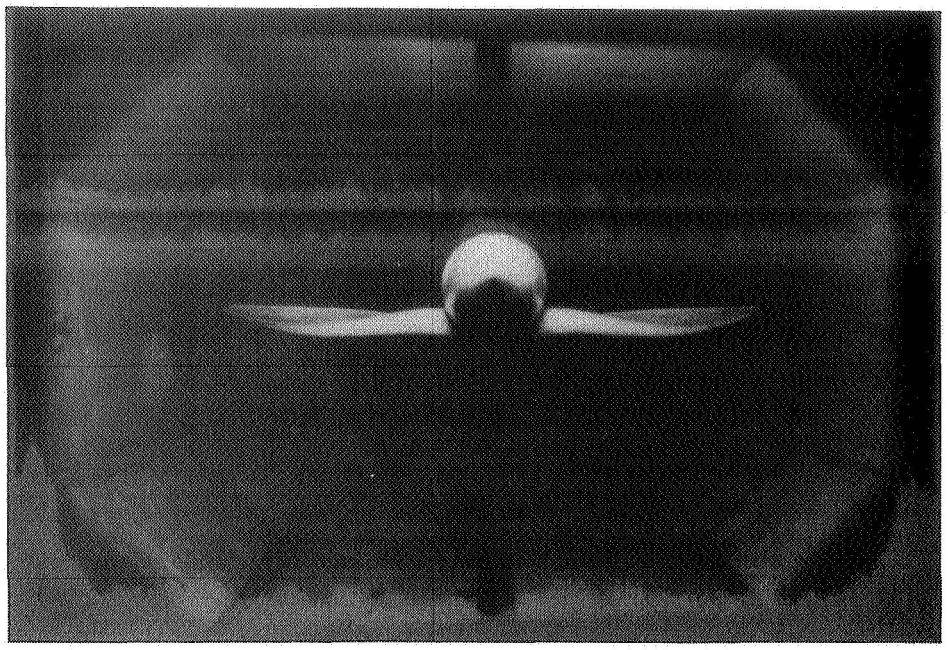

Figure 6.- Cambered-twisted wing without fin in the Boeing Transonic Wind Tunnel.

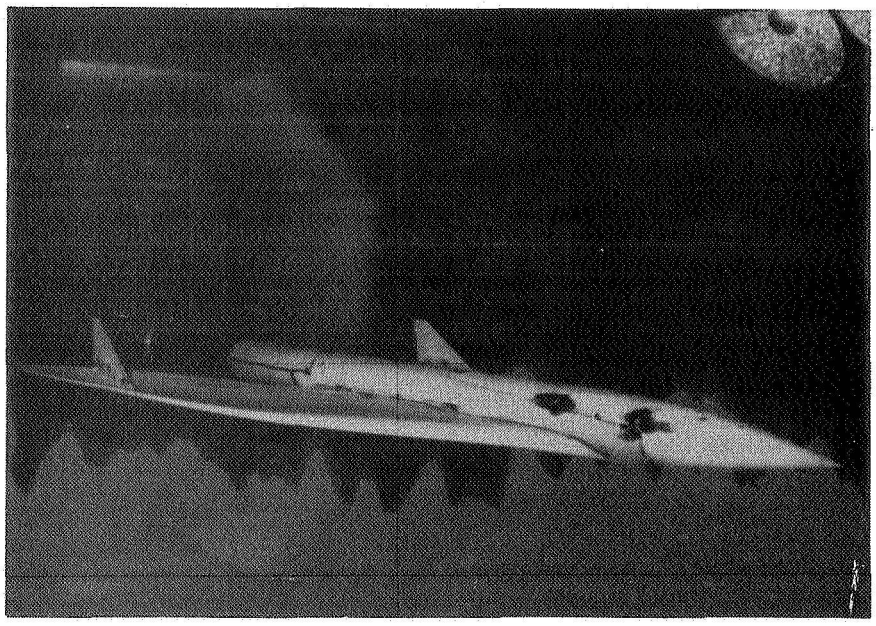

Figure 7.- Cambered-twisted wing with fin in the Boeing Transonic Wind Tunnel.

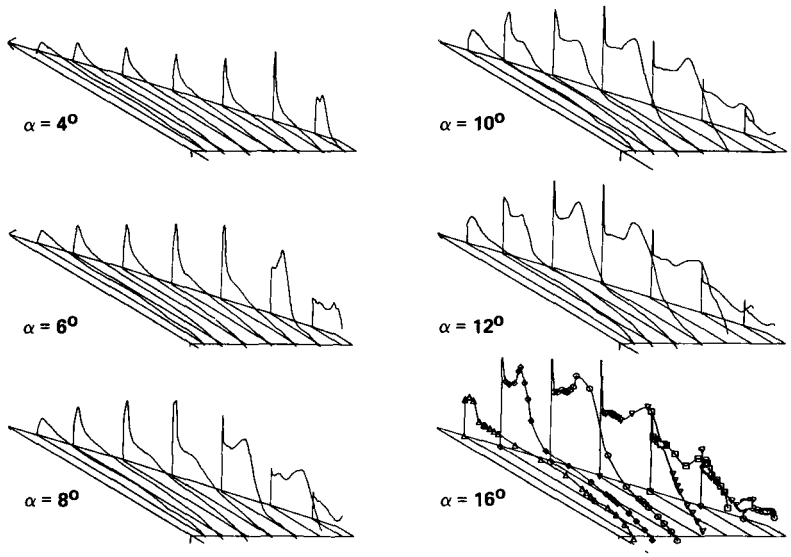

Figure 8.- Upper surface pressure distributions, rounded-leading-edge flat wing, M = 0.40.

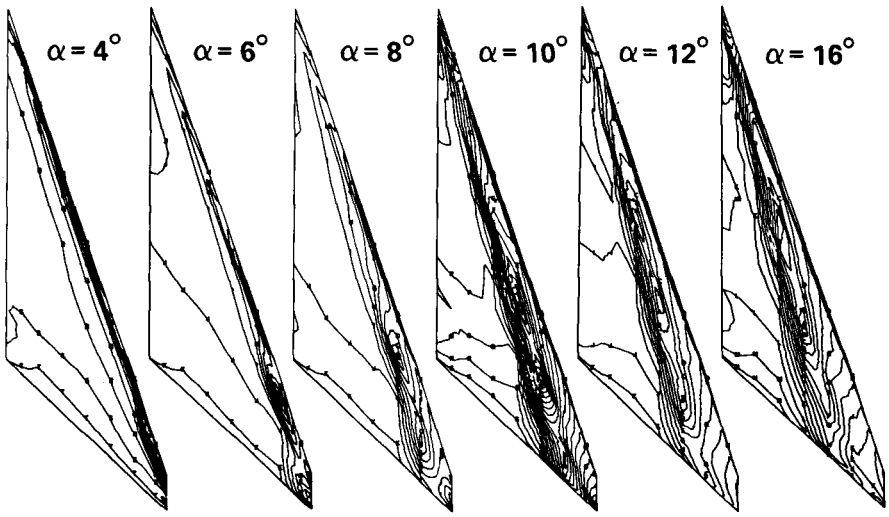

Figure 9.- Upper surface isobars, rounded-leading-edge flat wing, M = 0.40.

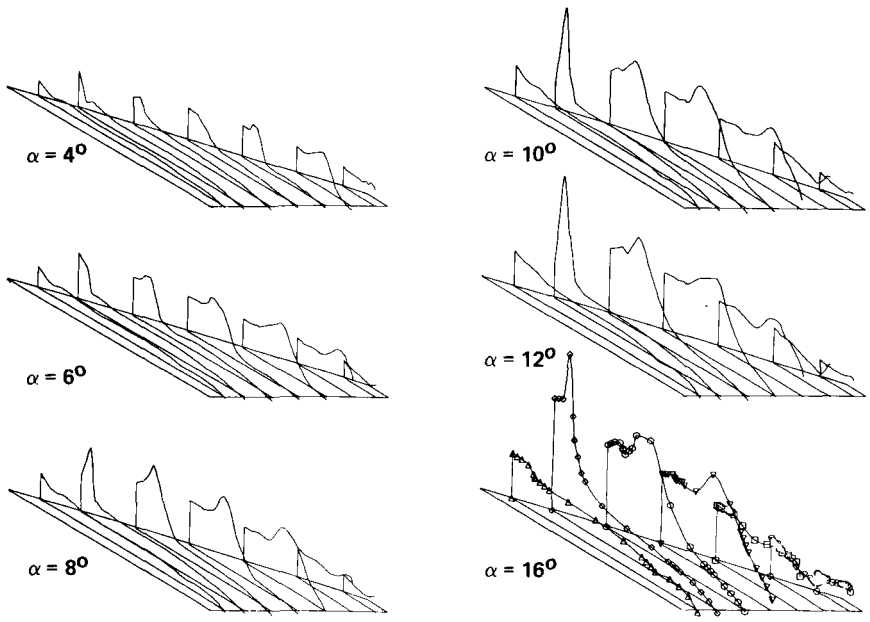

Figure 10.- Upper surface pressure distributions, sharp-leading-edge flat wing, M = 0.40.

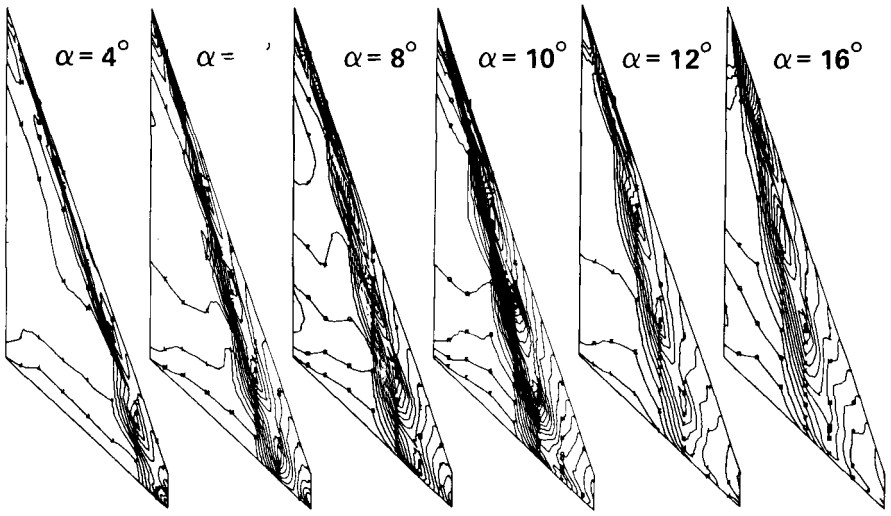

Figure 11.- Upper surface isobars, sharp-leading-edge flat wing, M = 0.40.

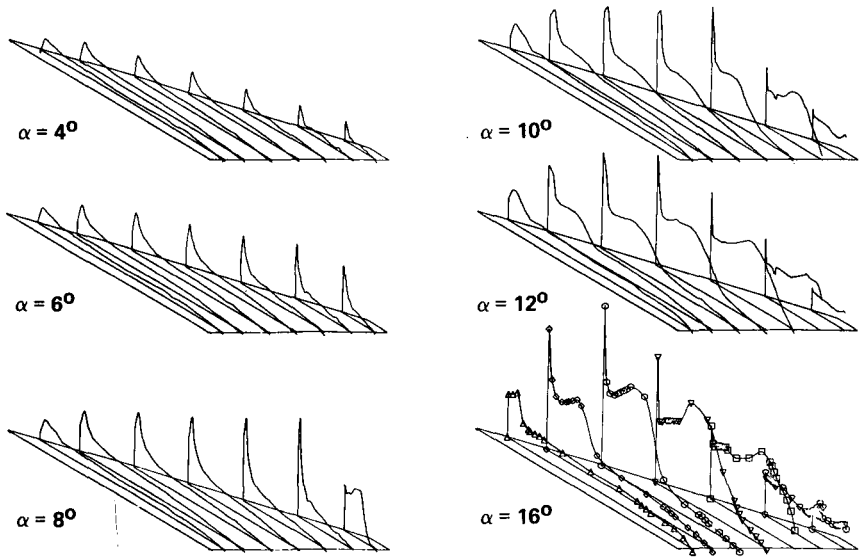

Figure 12.- Upper surface pressure distributions, rounded-leading-edge twisted wing, M = 0.40.

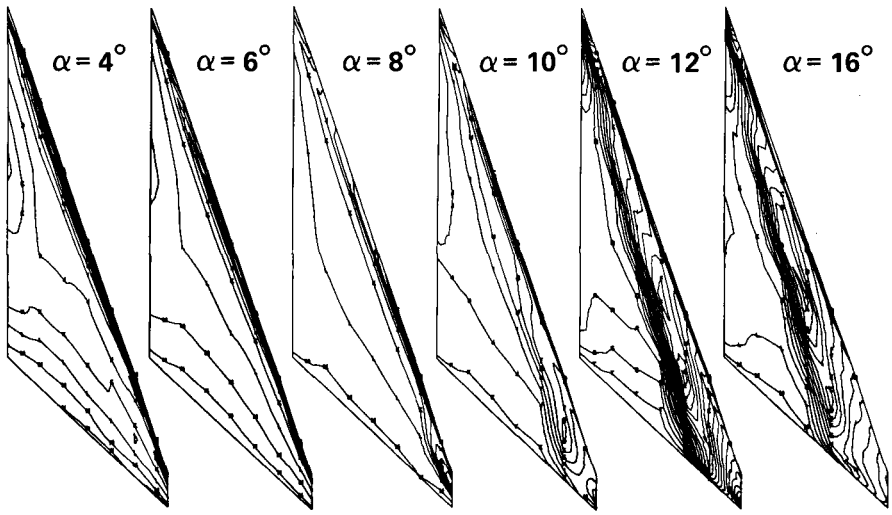

Figure 13.- Upper surface isobars, rounded-leading-edge twisted wing, M = 0.40.

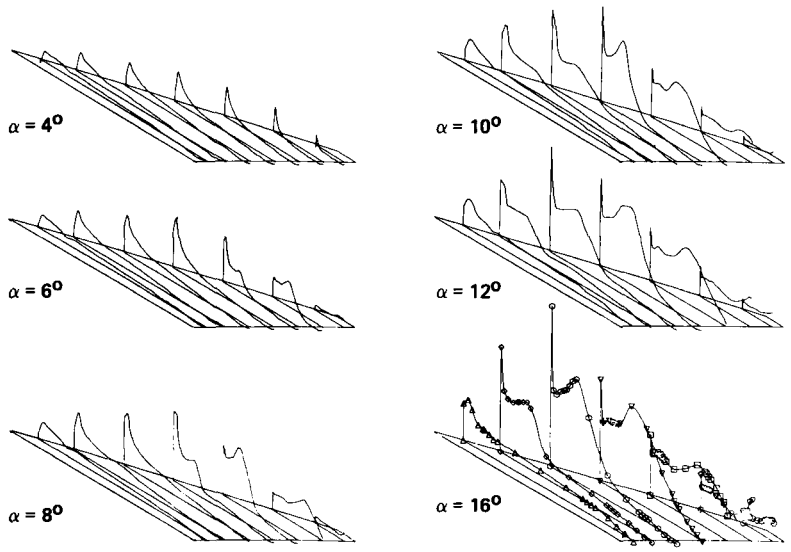

Figure 14.- Upper surface pressure distributions, rounded-leading-edge cambered-twisted wing, fin off, M = 0.40.

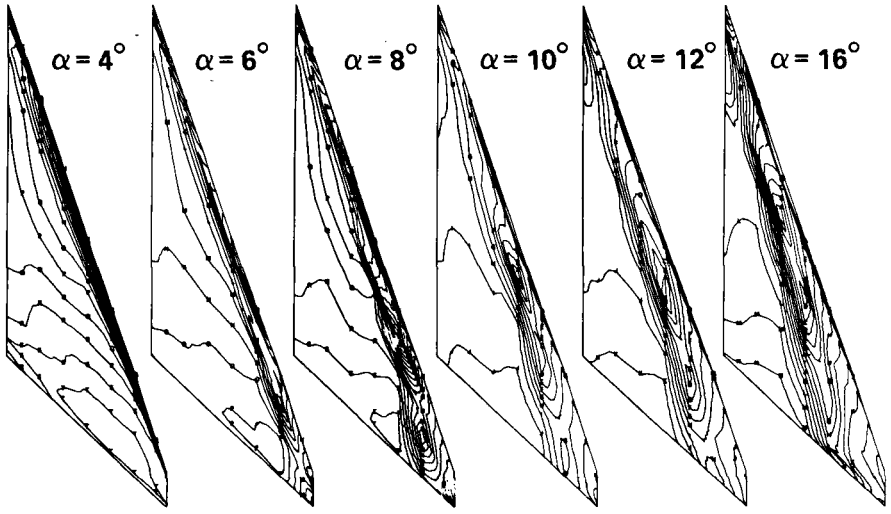

Figure 15.- Upper surface isobars, rounded-leading-edge cambered-twisted wing, fin off, M = 0.40.

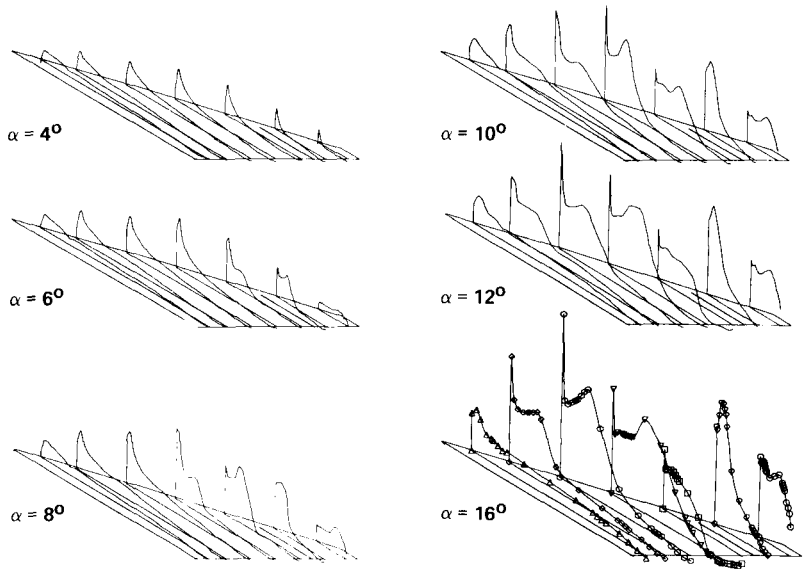

Figure 16.- Upper surface pressure distributions, rounded-leading-edge cambered-twisted wing, fin on, M = 0.40.

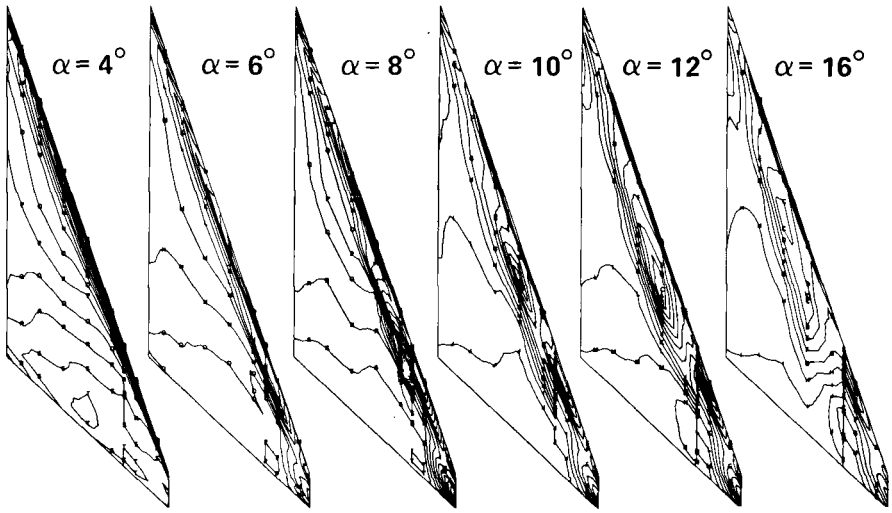

Figure 17.- Upper surface isobars, rounded-leading-edge cambered-twisted wing, fin on, M = 0.40.

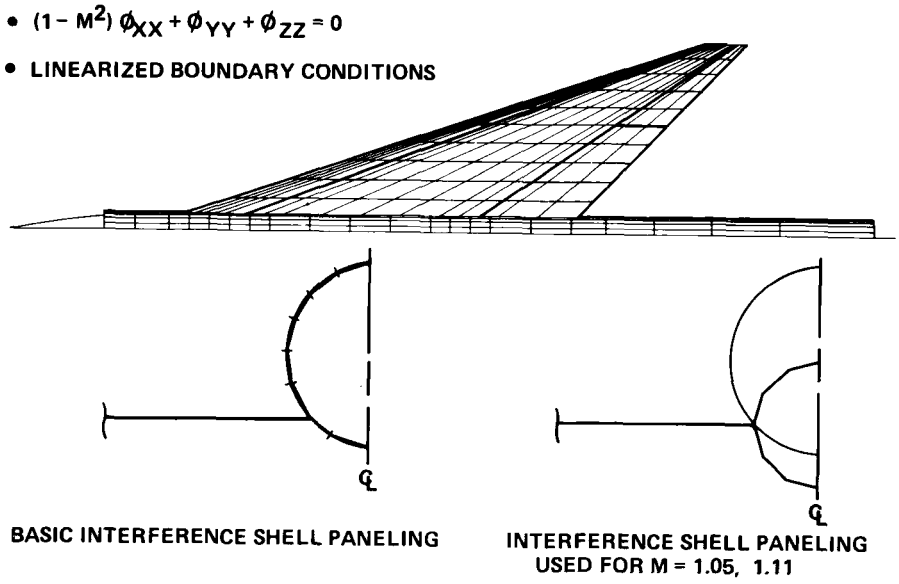

Figure 18.- FLEXSTAB paneling scheme.

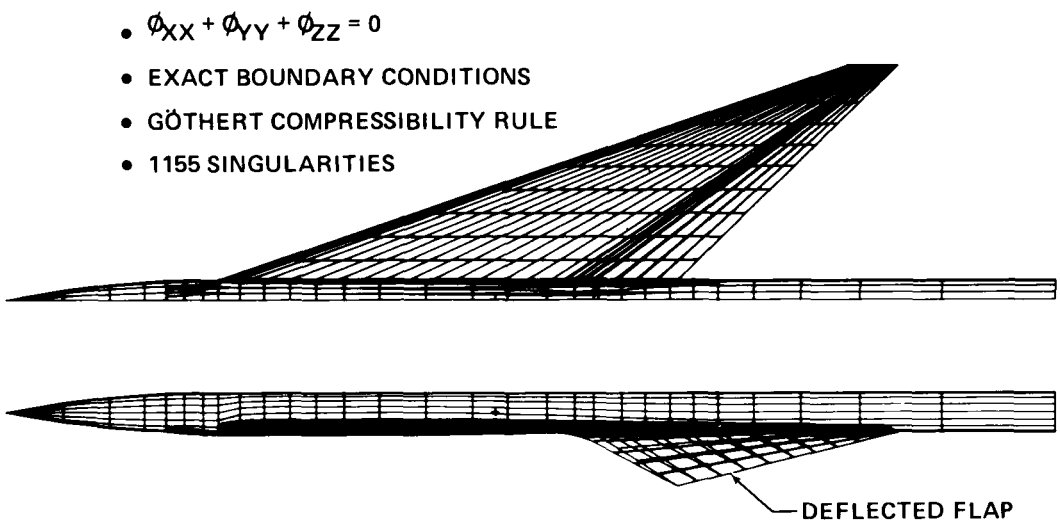

Figure 19.- TEA-230 paneling scheme.

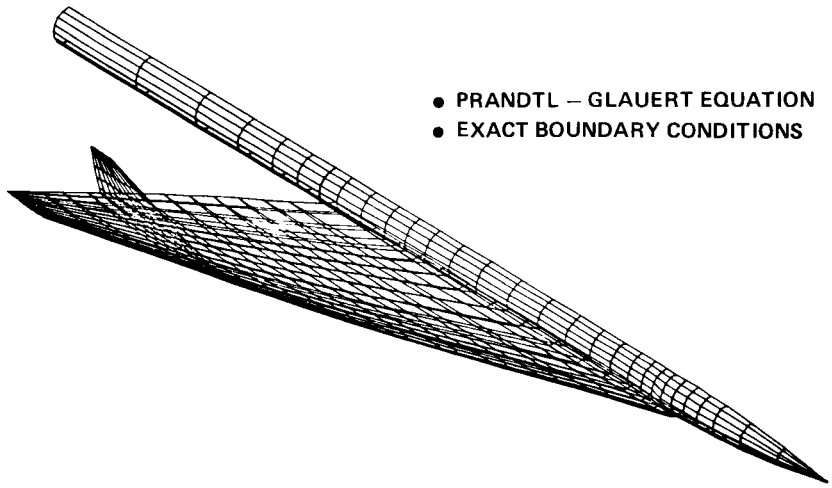

Figure 20.- PANAIR paneling scheme.

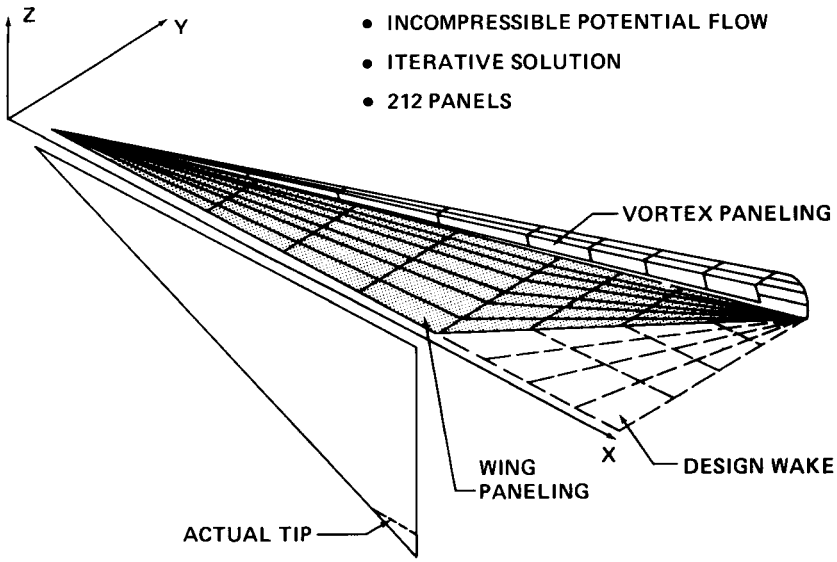

Figure 21.- Leading edge vortex (LEV) program paneling scheme.

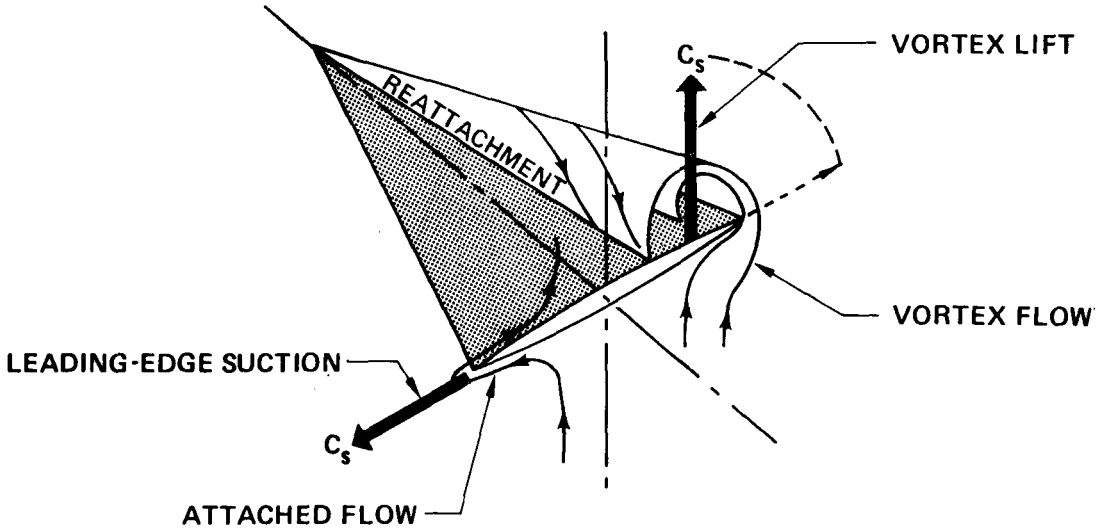

Figure 22.- Leading edge suction analogy — thin, sharp-leading-edge wings.

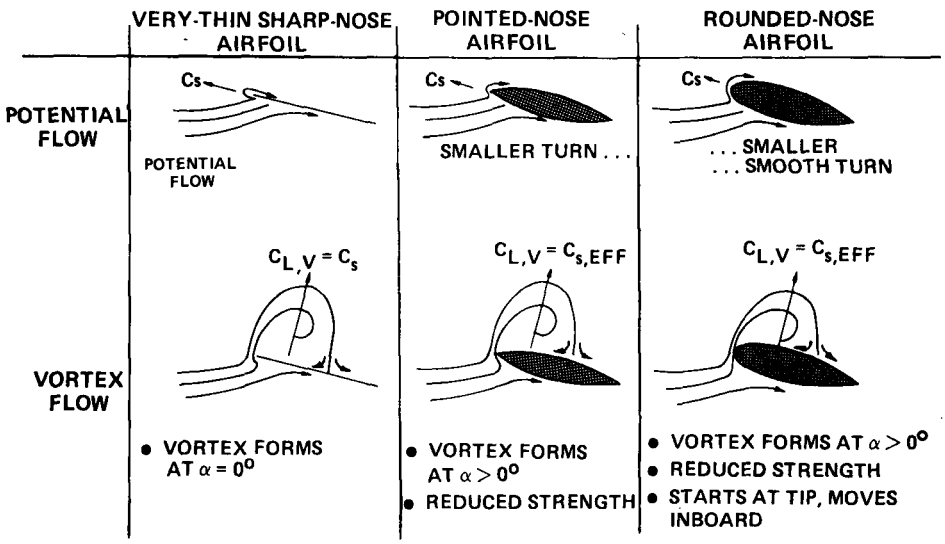

Figure 23.- Effect of airfoil shape on the vortex lift of a highly-swept wing.

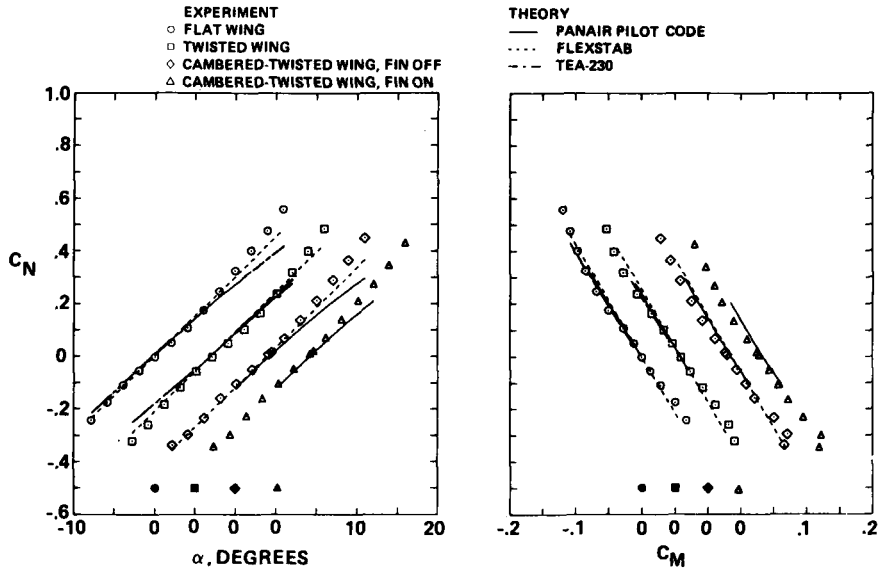

Figure 24.- Wing normal force and pitching moment coefficients, M = 0.40.

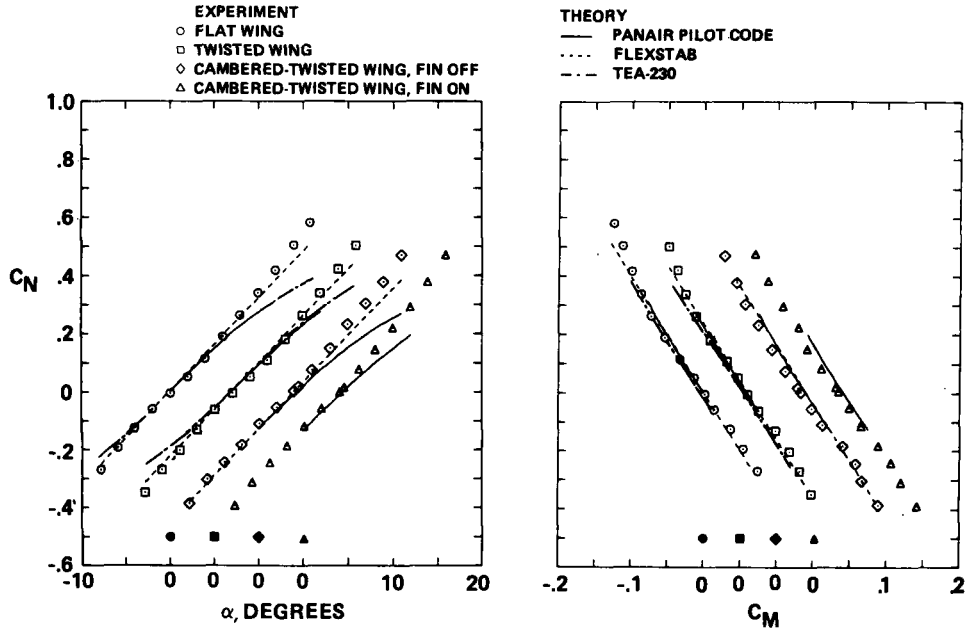

Figure 25.- Wing normal force and pitching moment coefficients, M = 0.85.

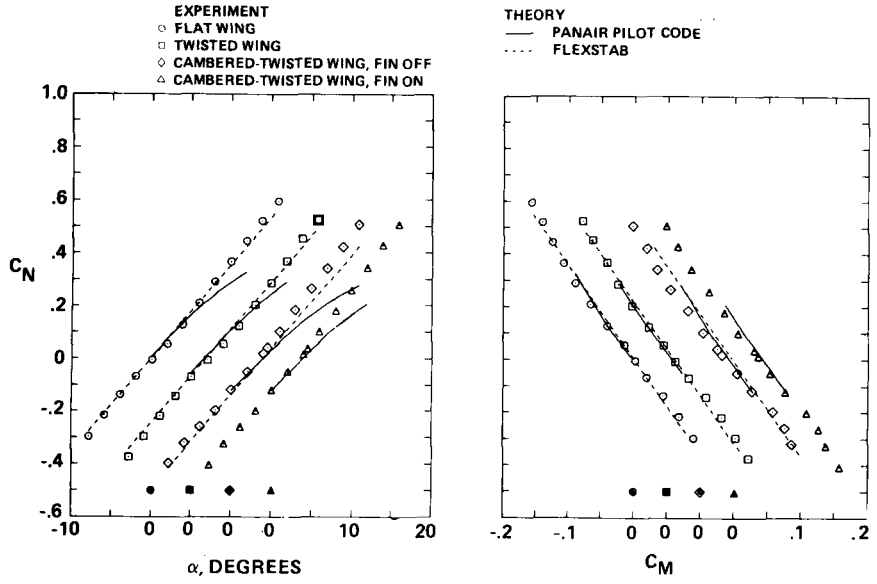

Figure 26.- Wing normal force and pitching moment coefficients, M = 1.05.

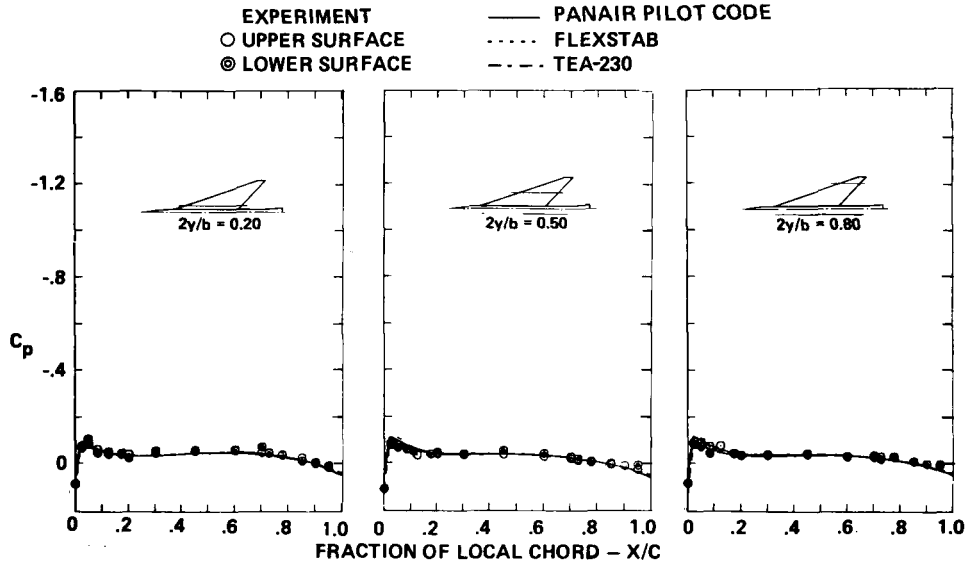

Figure 27.- Surface pressure distributions, flat wing, M = 0.40, $\alpha = 0^{o}$.

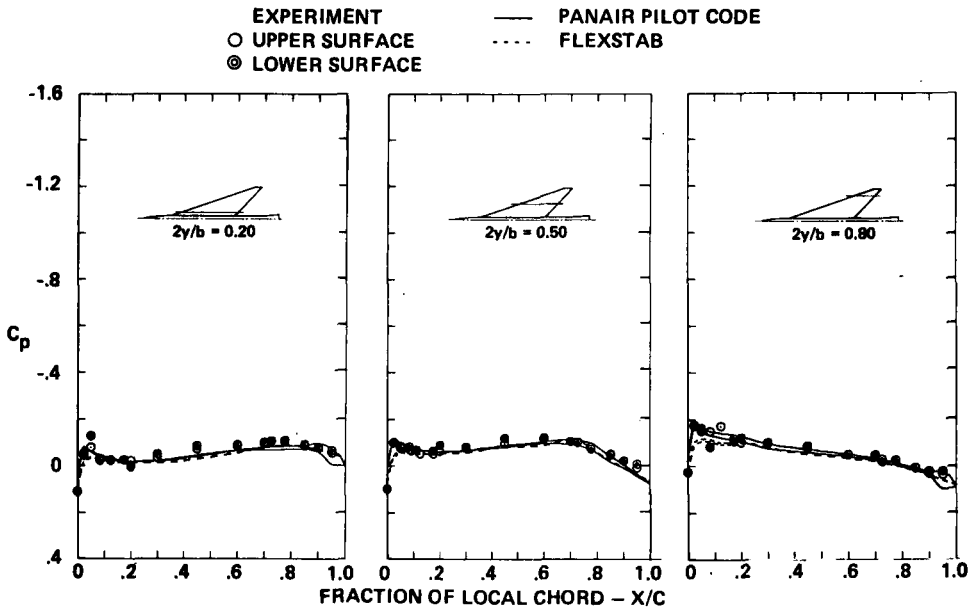

Figure 28.- Surface pressure distributions, flat wing, $M = 1.05$, $\alpha = 0^{\circ}$.

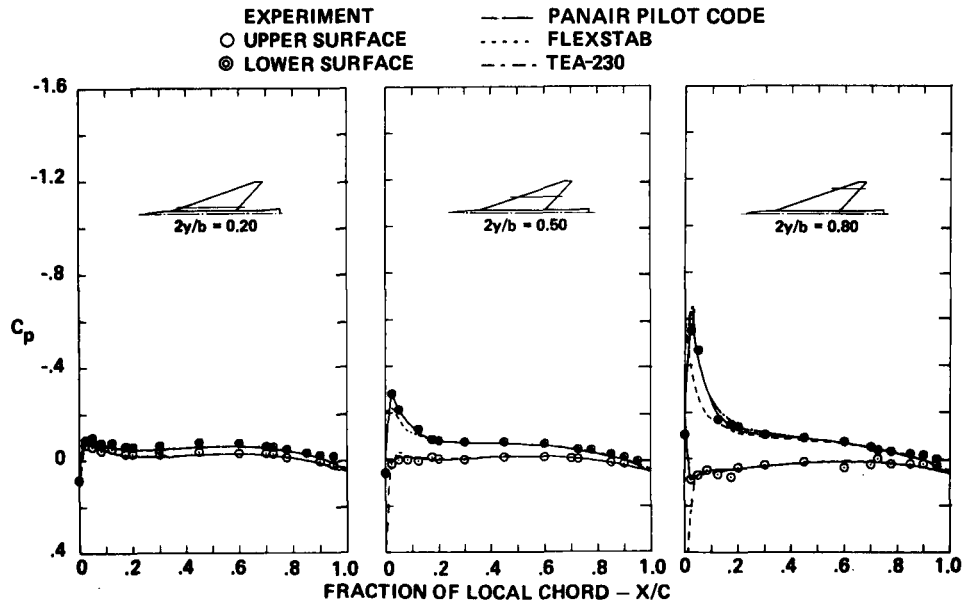

Figure 29.- Surface pressure distributions, twisted wing, $M = 0.40$, $\alpha = 0^{\circ}$.

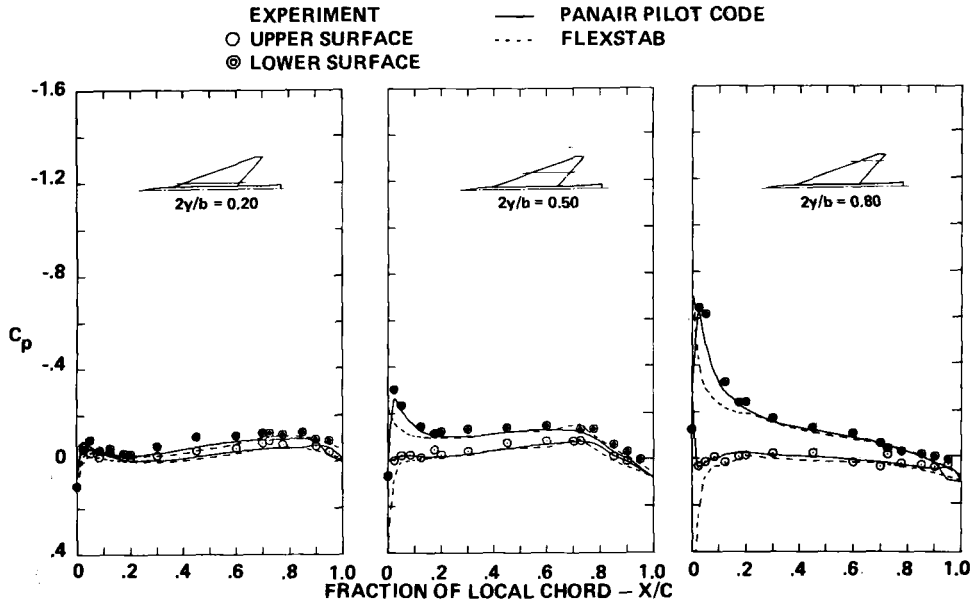

Figure 30.- Surface pressure distributions, twisted wing, M = 1.05, $\alpha = 0^{o}$.

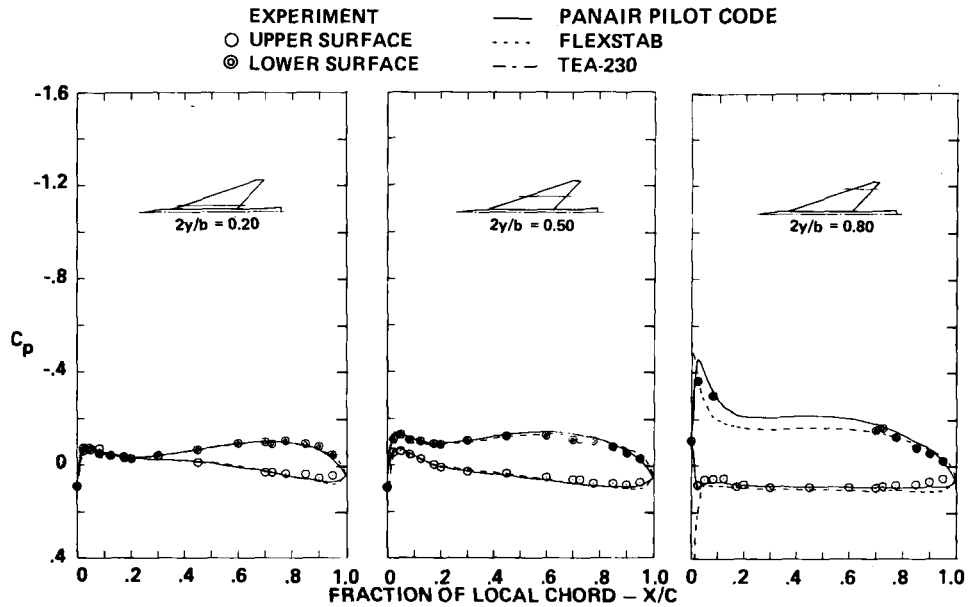

Figure 31.- Surface pressure distributions, cambered-twisted wing, fin off, M = 0.40, $\alpha = 0^{o}$.

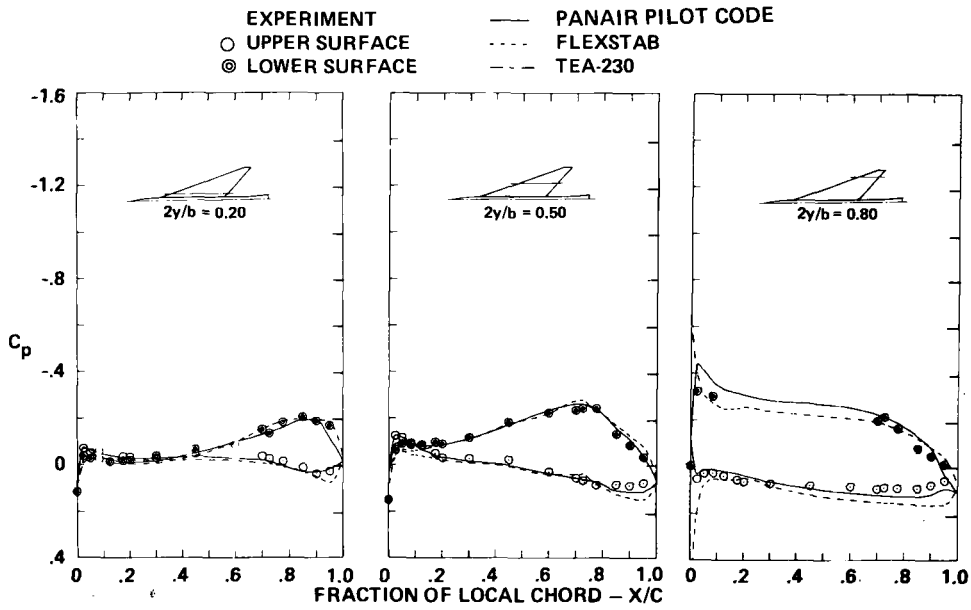

Figure 32.- Surface pressure distributions, cambered-twisted wing, fin off, M = 1.05, $\alpha = 0^{o}$.

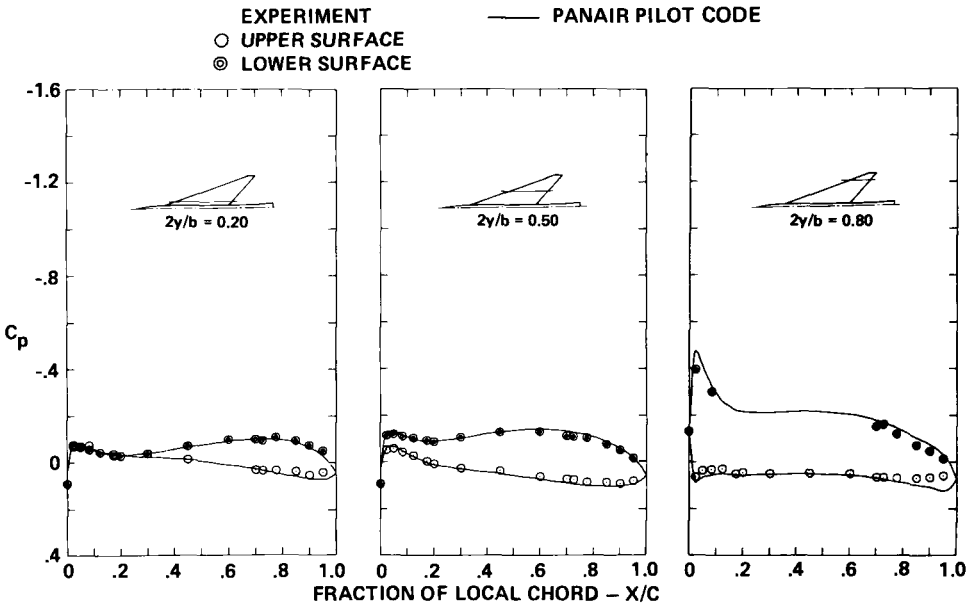

Figure 33.- Surface pressure distributions, cambered-twisted wing, fin on, M = 0.40, $\alpha = 0^{o}$.

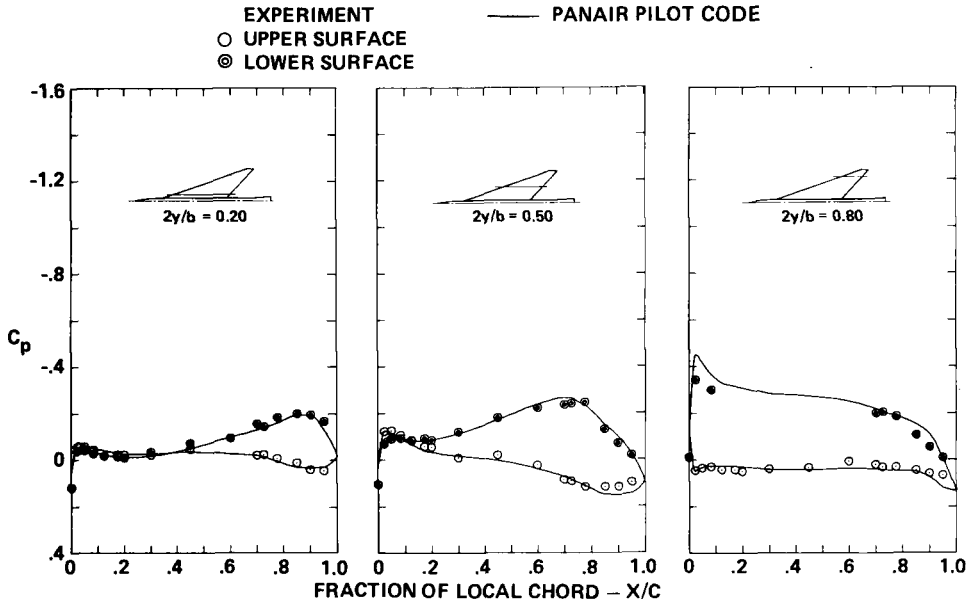

Figure 34.- Surface pressure distributions, cambered-twisted wing, fin on, M = 1.05, $\alpha = 0^{\circ}$.

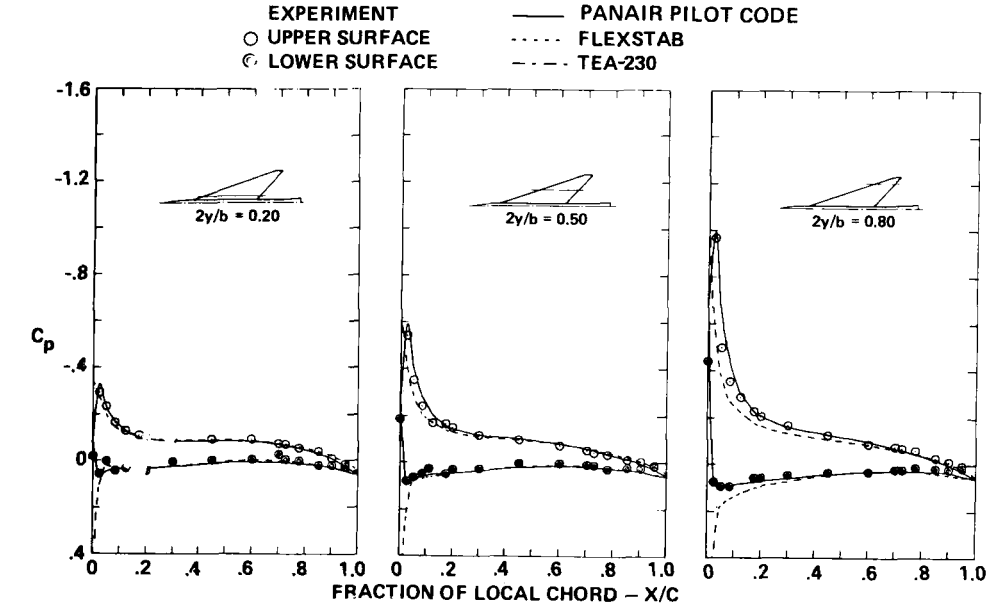

Figure 35.- Surface pressure distributions, flat wing, M = 0.40, $\alpha = 4^{\circ}$.

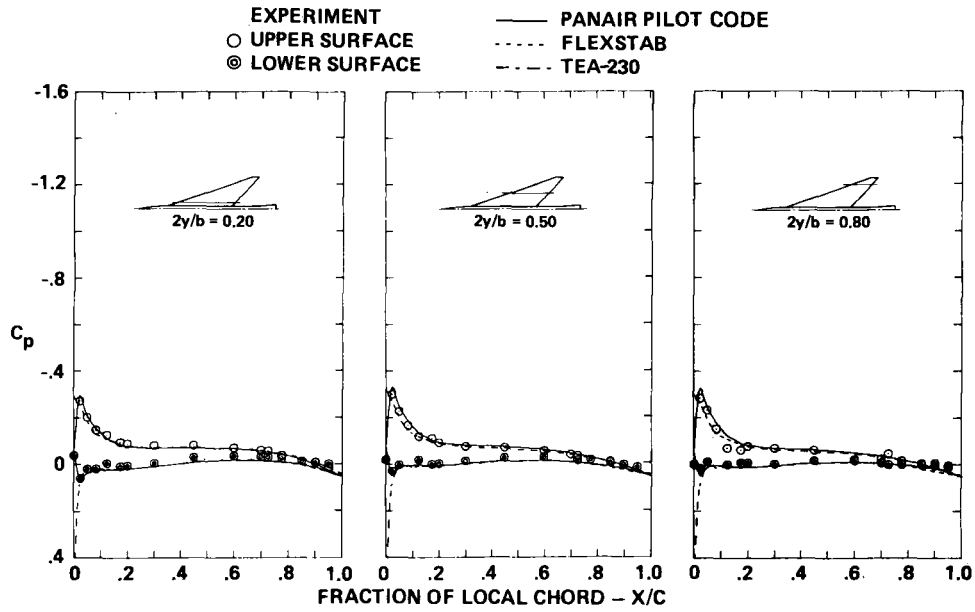

Figure 36.- Surface pressure distributions, twisted wing, M = 0.40, $\alpha = 4^{o}$.

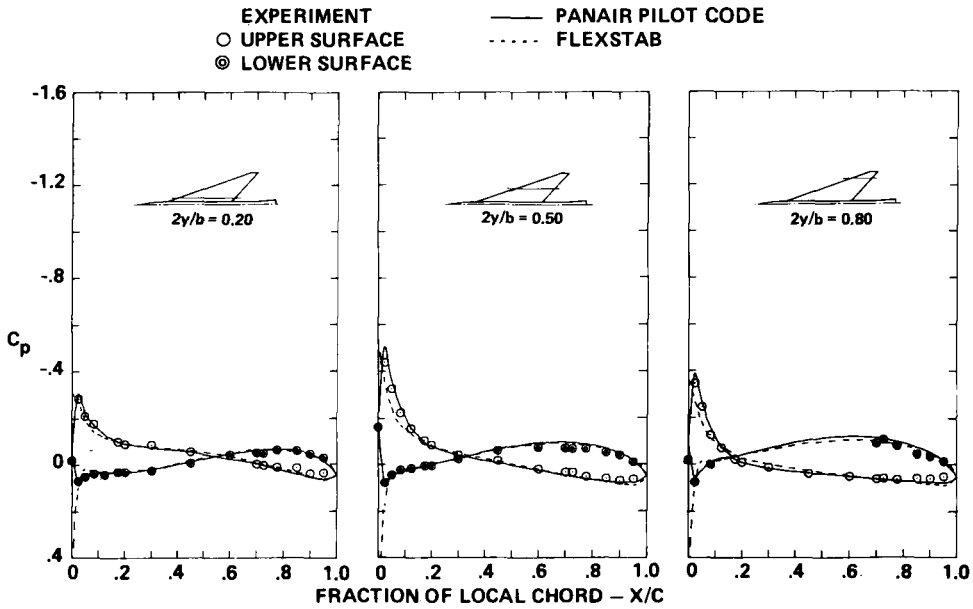

Figure 37.- Surface pressure distributions, cambered-twisted wing, fin off, M = 0.40, $\alpha = 4^{o}$.

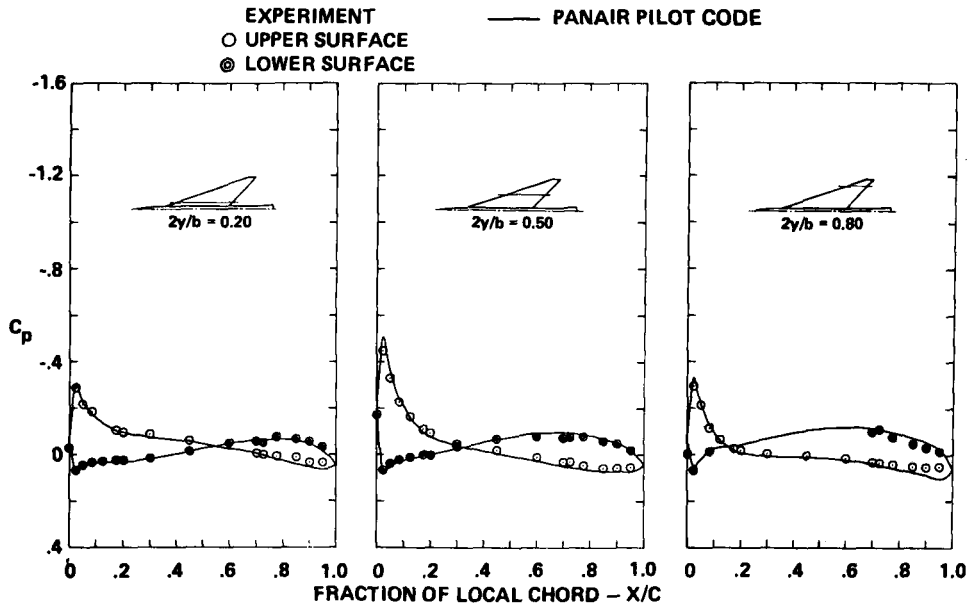

Figure 38.- Surface pressure distributions, cambered-twisted wing, fin on, M = 0.40, $\alpha = 4^{o}$.

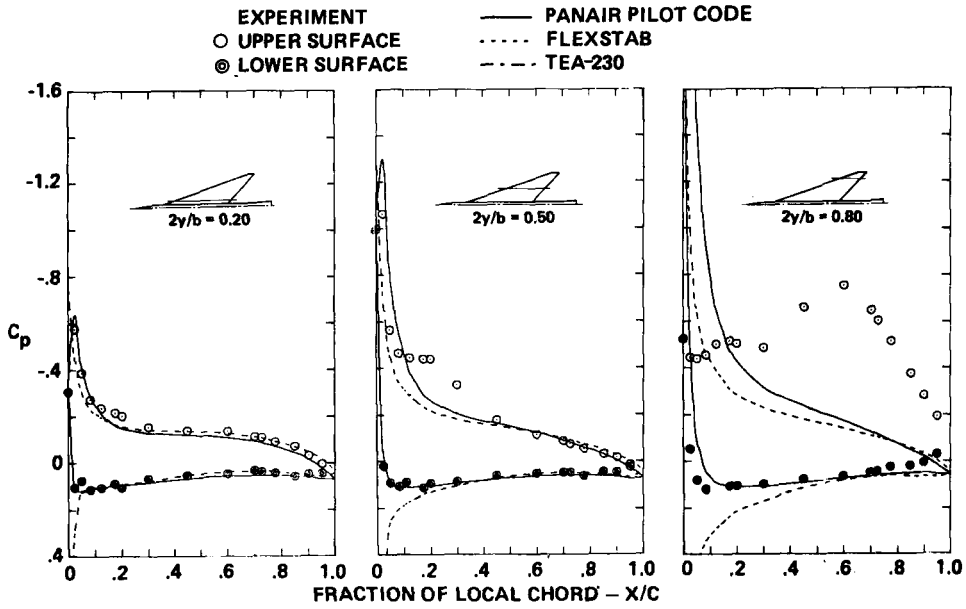

Figure 39.- Surface pressure distributions, flat wing, M = 0.40, $\alpha = 8^{o}$.

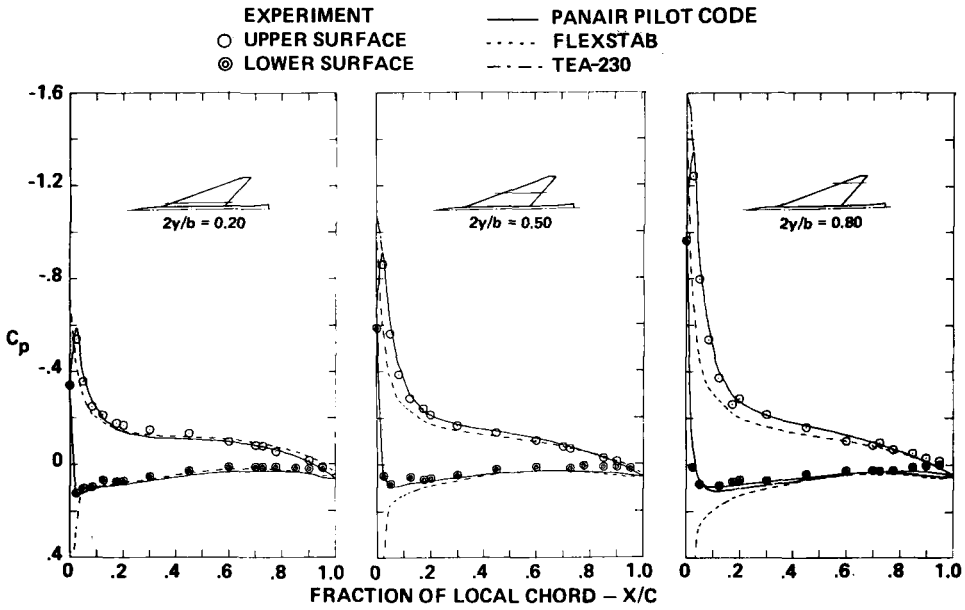

Figure 40.- Surface pressure distributions, twisted wing, M = 0.40, $\alpha = 8^{o}$.

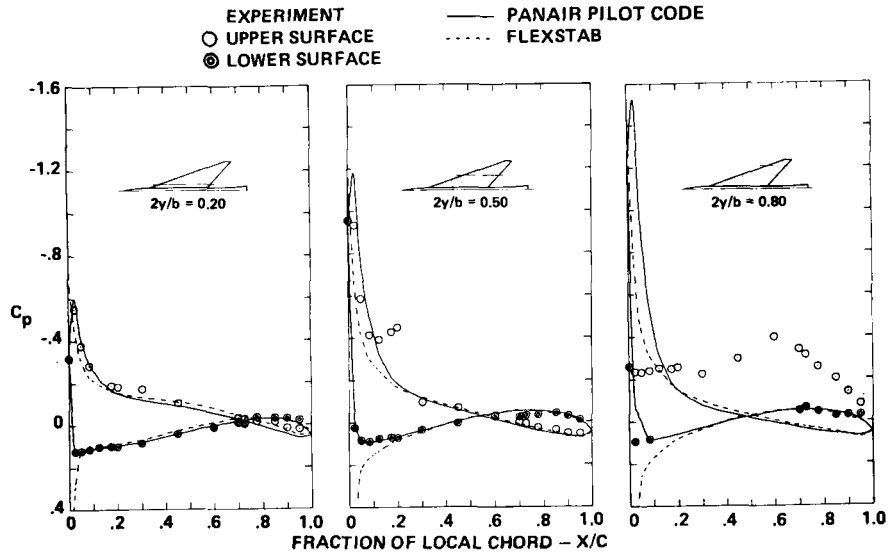

Figure 41.- Surface pressure distributions, cambered-twisted wing, fin off, M = 0.40, $\alpha = 8^{o}$.

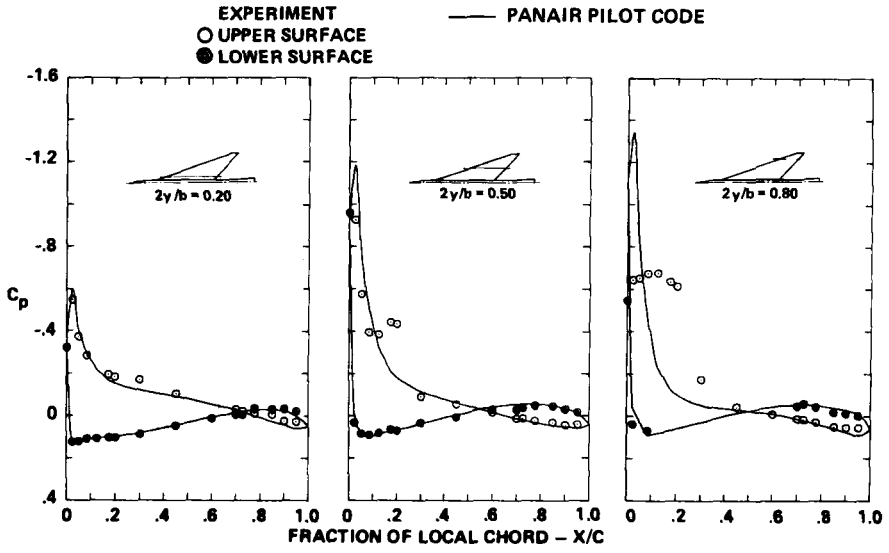

Figure 42.- Surface pressure distributions, cambered-twisted wing, fin on, $M = 0.40$, $\alpha = 8^{\circ}$.

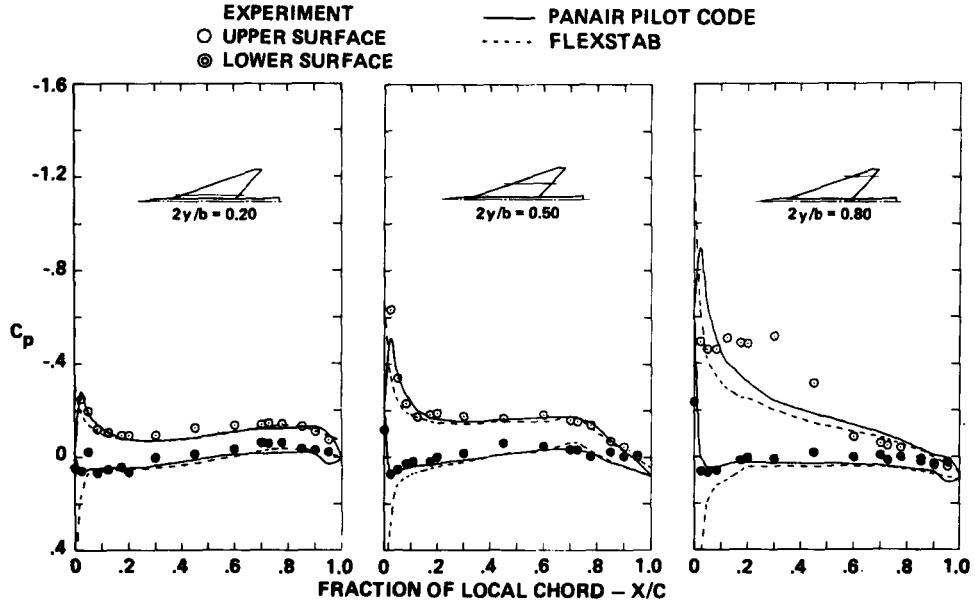

Figure 43.- Surface pressure distributions, flat wing, $M = 1.05$, $\alpha = 4^{\circ}$.

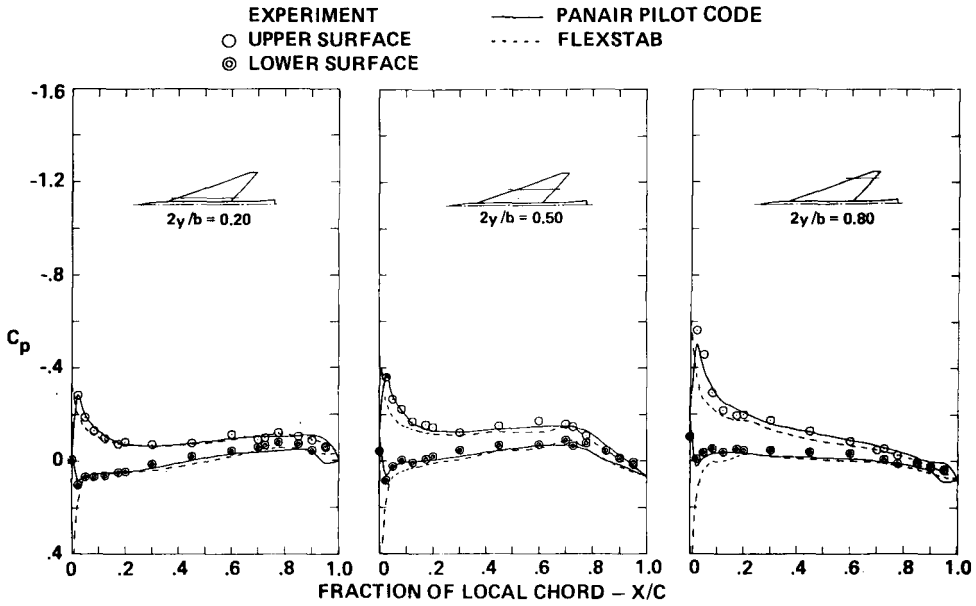

Figure 44.- Surface pressure distributions, twisted wing, M = 1.05, $\alpha = 4.5^{o}$.

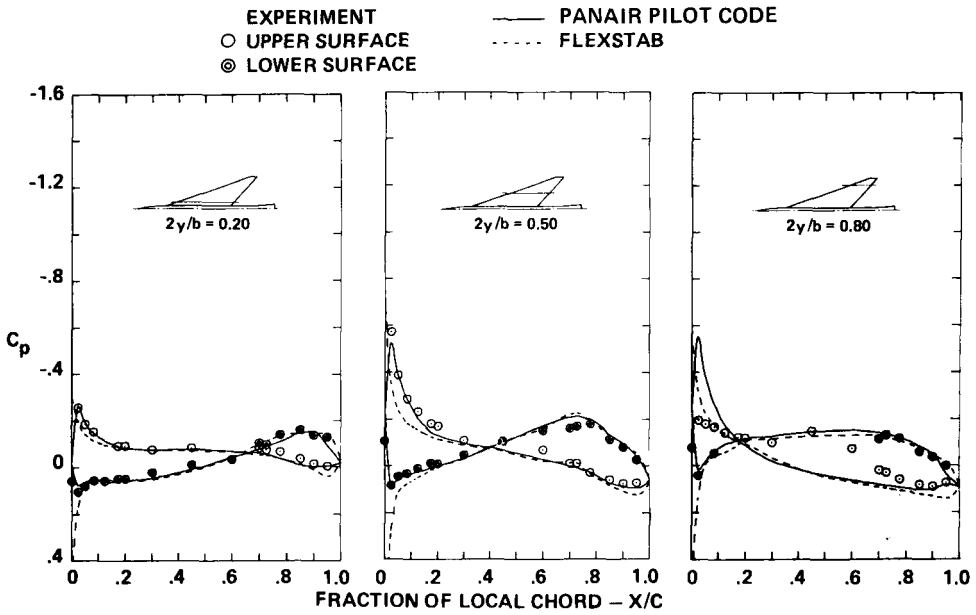

Figure 45.- Surface pressure distributions, cambered-twisted wing, fin off, M = 1.05, $\alpha = 4^{o}$.

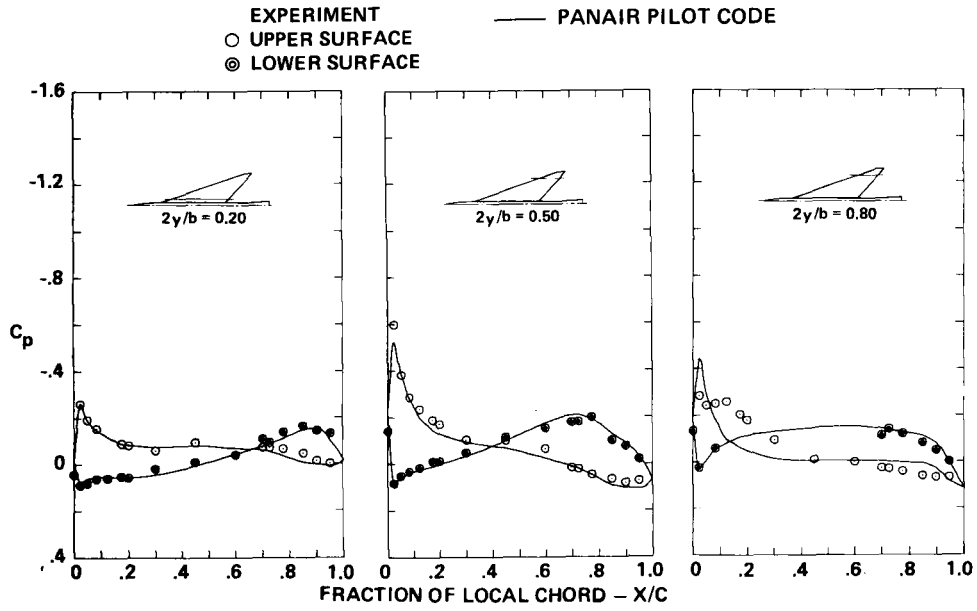

Figure 46.- Surface pressure distributions, cambered-twisted wing, fin on, M = 1.05, $\alpha = 4^{o}$.

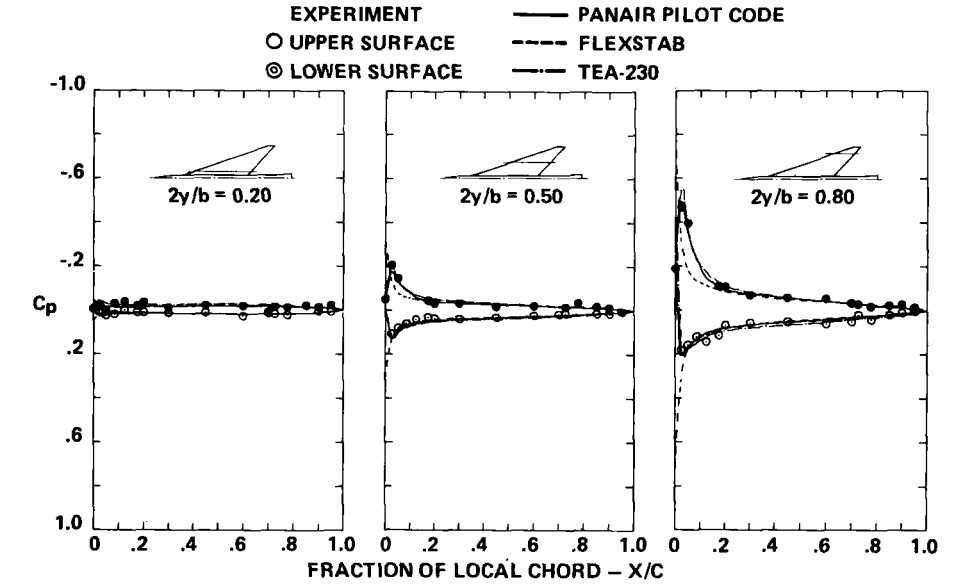

Figure 47.- Incremental surface pressure distributions due to twist, M = 0.40, $\alpha = 0^{o}$.

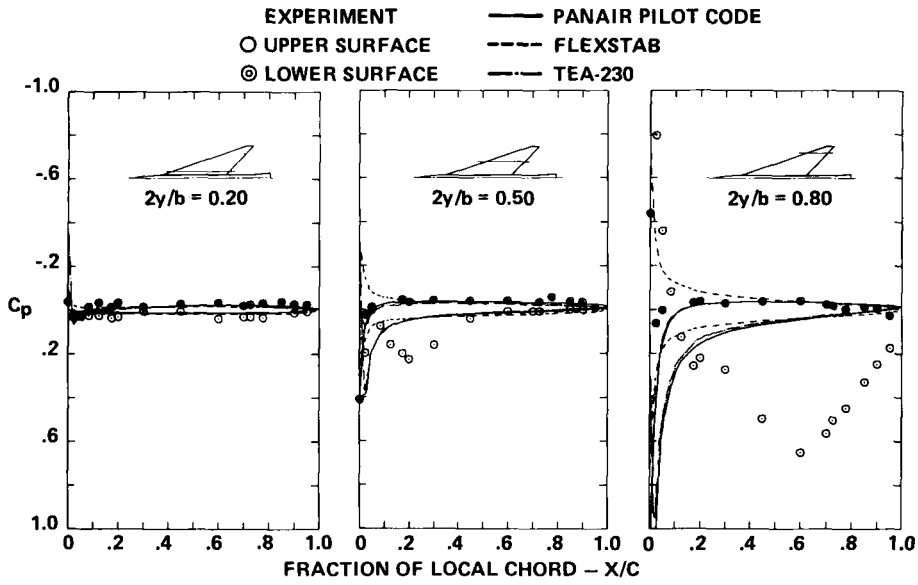

Figure 48.- Incremental surface pressure distributions due to twist, $M = 0.40$, $\alpha = 8^{o}$.

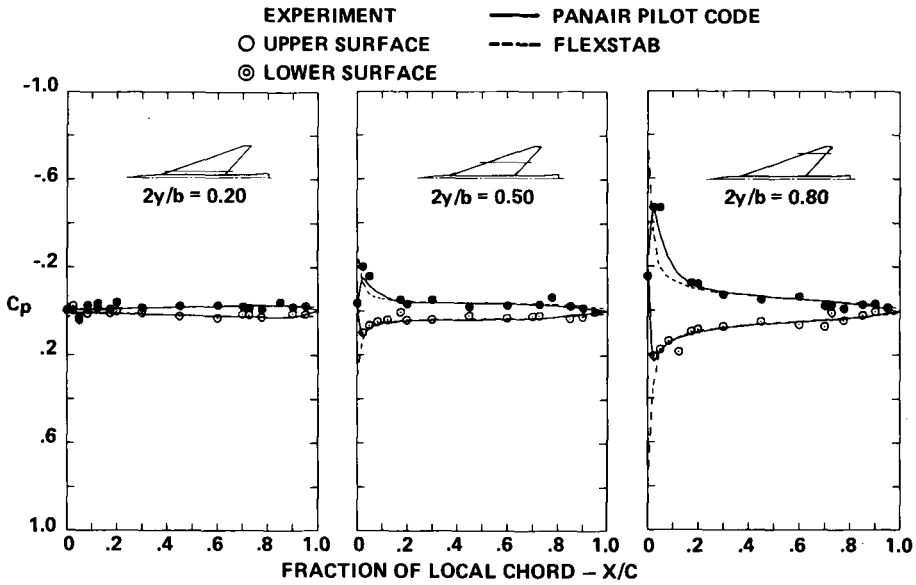

Figure 49.- Incremental surface pressure distributions due to twist, $M = 1.05$, $\alpha = 0^{o}$.

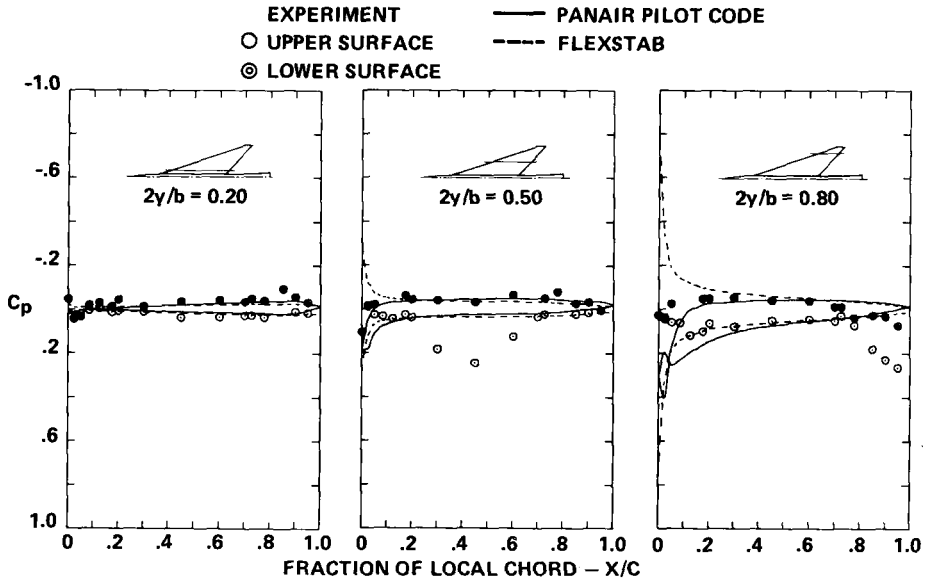

Figure 50 - Incremental surface pressure distributions due to twist, M = 1.05, $\alpha = 8^{o}$.

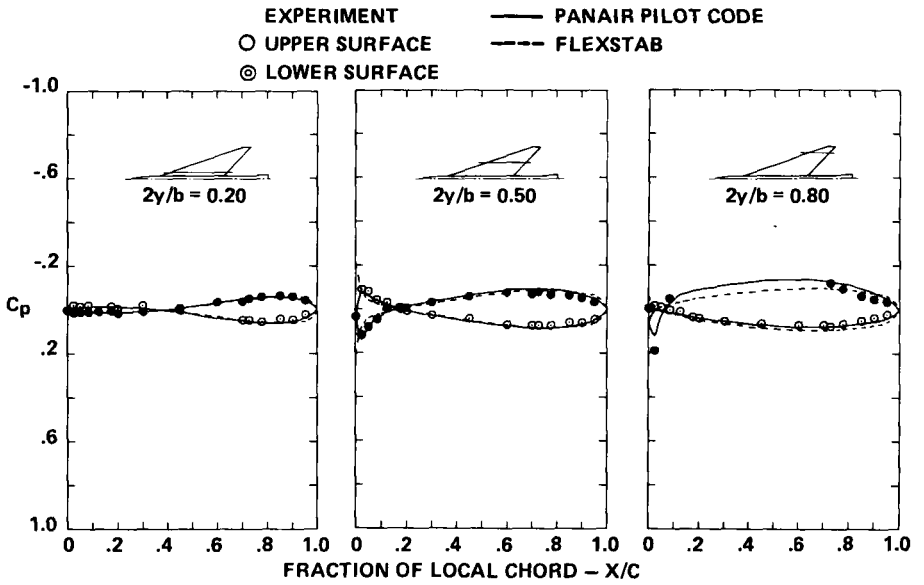

Figure 51.- Incremental surface pressure distributions due to camber, M = 0.40, $\alpha = 0^{o}$.

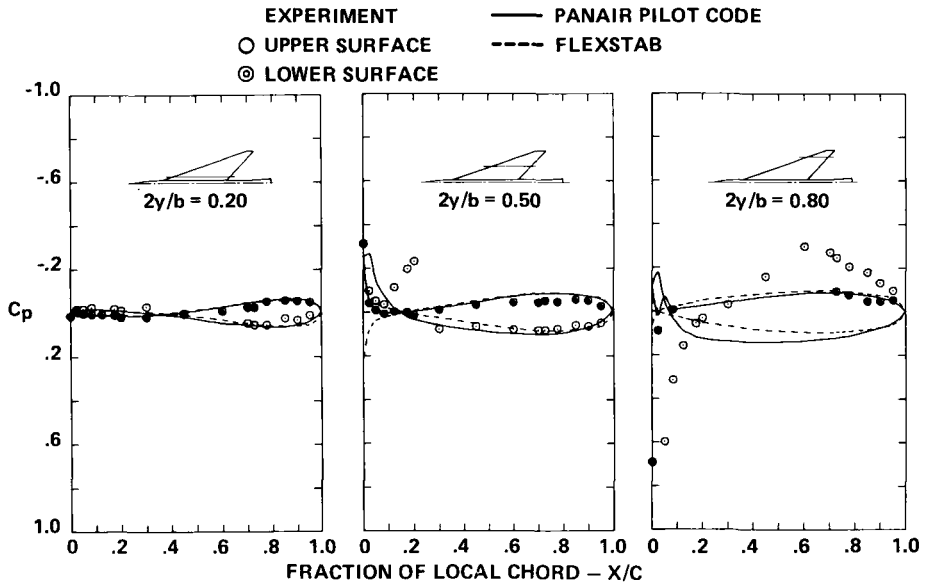

Figure 52.- Incremental surface pressure distributions due to camber, M = 0.40, $\alpha = 8^{o}$.

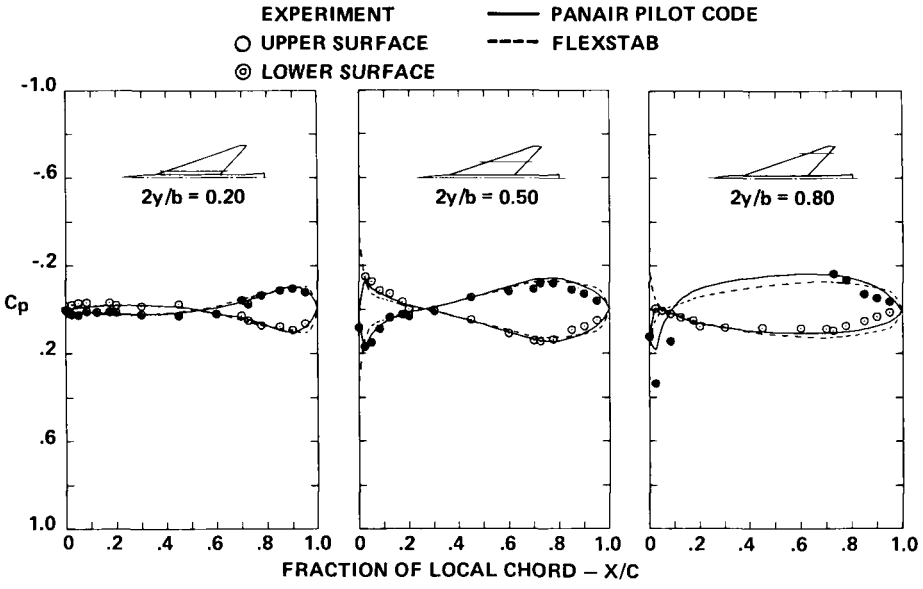

Figure 53.- Incremental surface pressure distributions due to camber, M = 1.05, $\alpha = 0^{o}$.

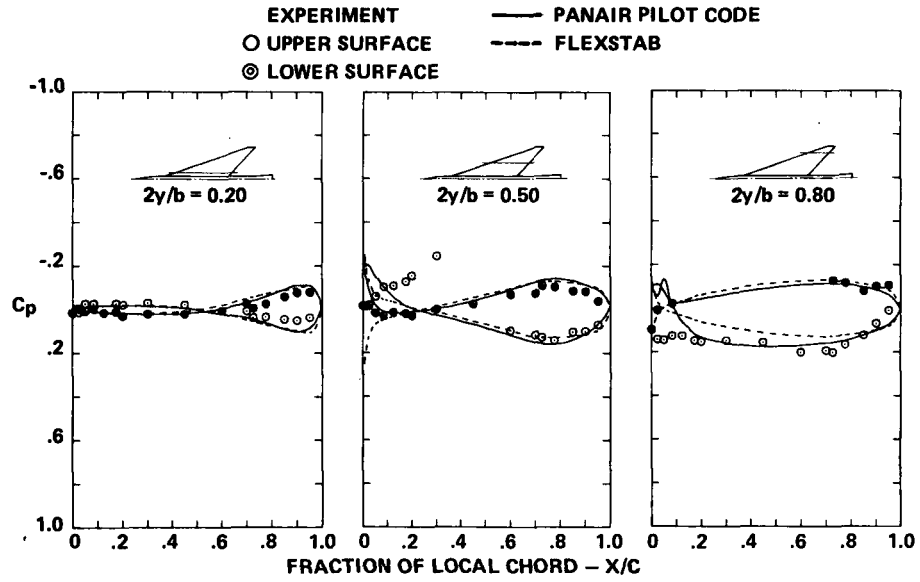

Figure 54.- Incremental surface pressure distributions due to camber, M = 1.05, $\alpha = 8^{o}$.

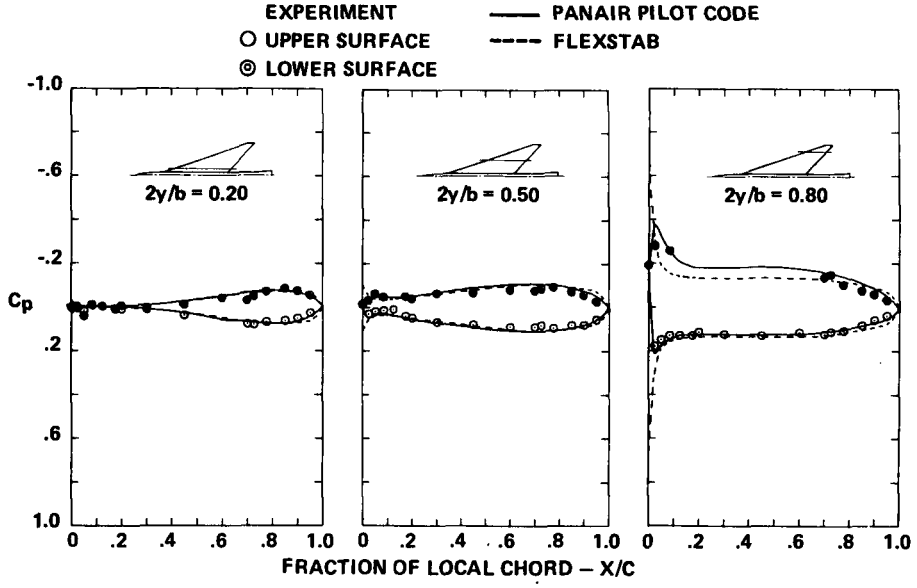

Figure 55.- Incremental surface pressure distributions due to camber and twist, M = 0.40, $\alpha = 0^{o}$.

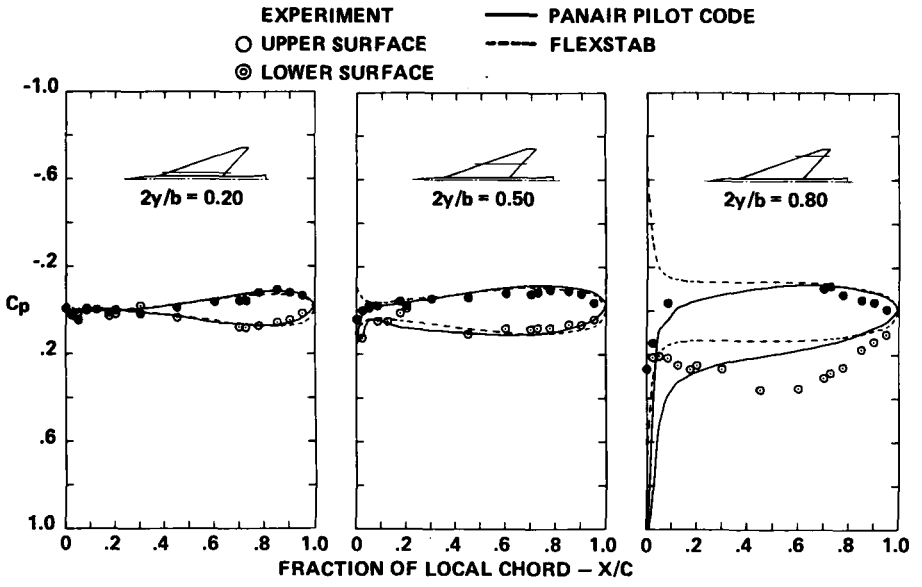

Figure 56.- Incremental surface pressure distributions due to camber and twist, M = 0.40, $\alpha = 8^{\circ}$

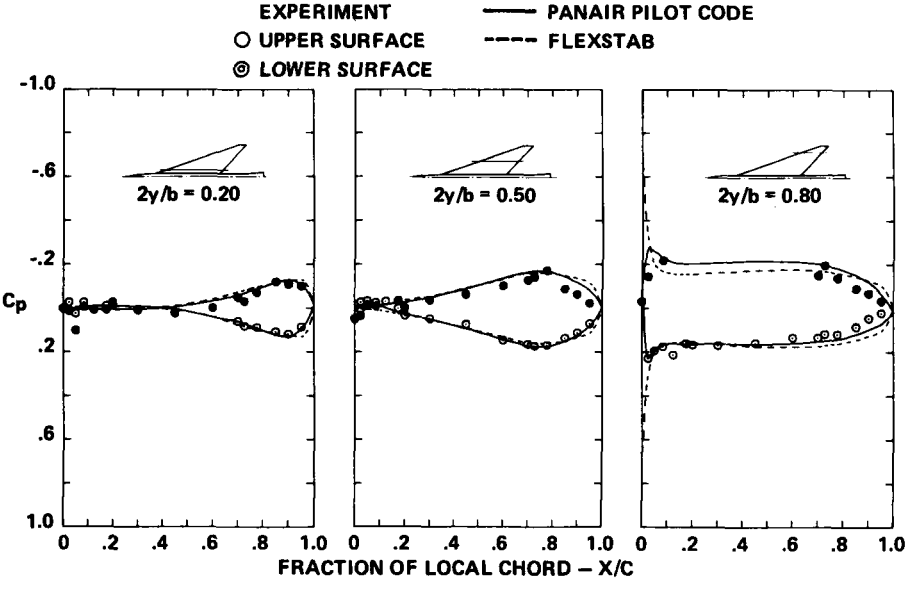

Figure 57.- Incremental surface pressure distributions due to camber and twist, M = 1.05, $\alpha = 0^{\circ}$.

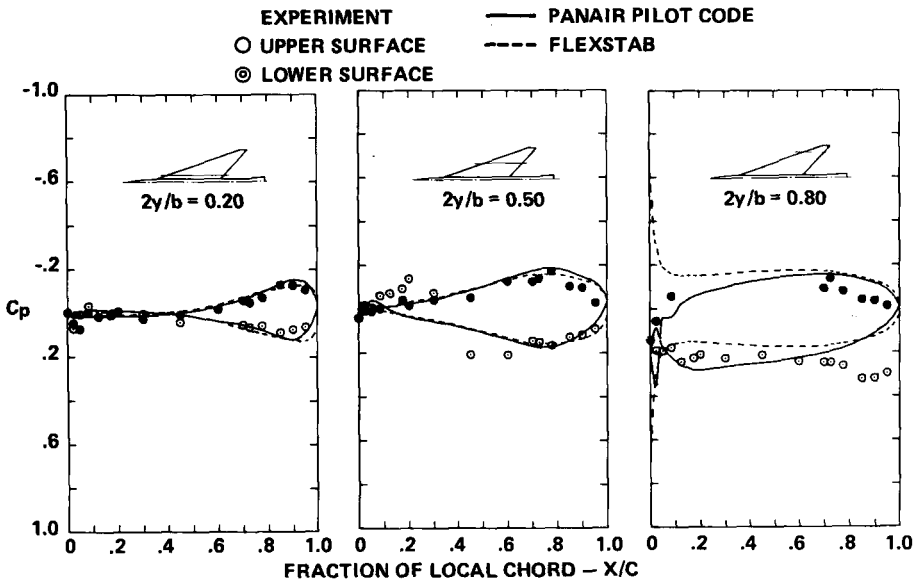

Figure 58.- Incremental surface pressure distributions due to camber and twist, M = 1.05, $\alpha = 8^{o}$.

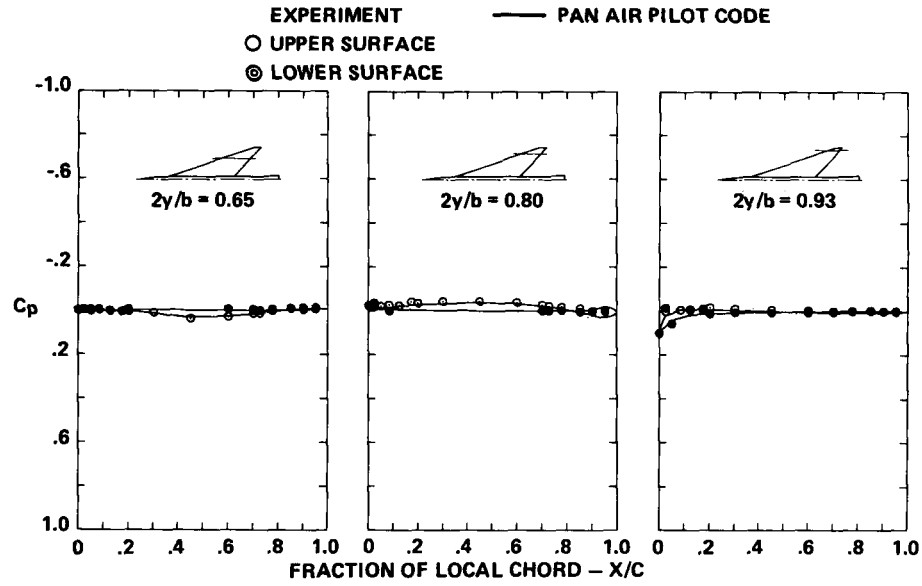

Figure 59.- Incremental surface pressure distributions due to a wing fin on the cambered-twisted wing, M = 0.40, $\alpha = 0^{o}$.

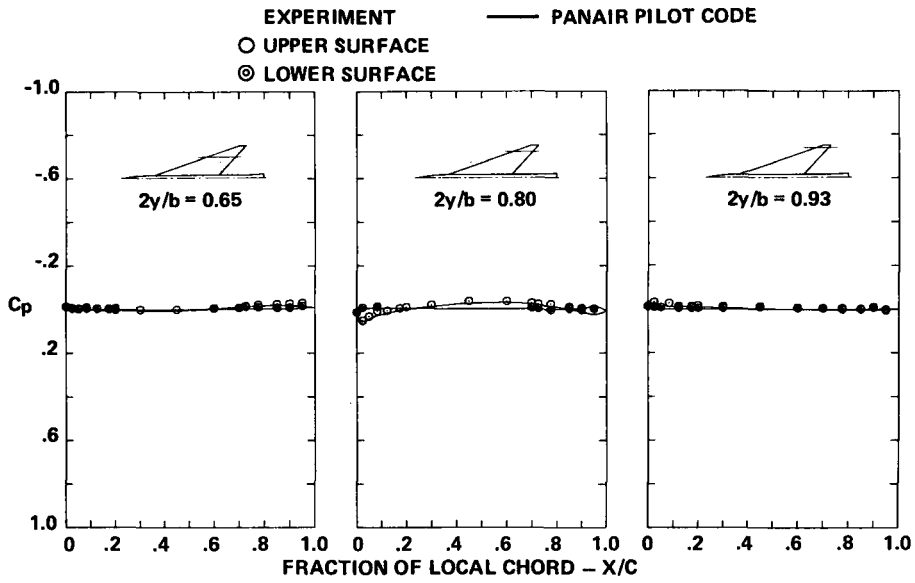

Figure 60.- Incremental surface pressure distributions due to a wing fin on the cambered-twisted wing, M = 0.40, $\alpha = 4^{o}$.

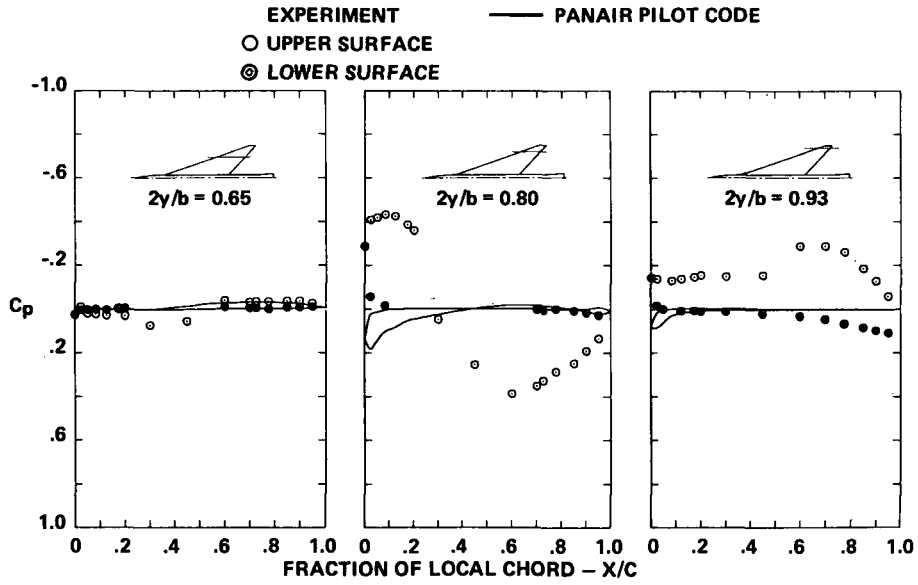

Figure 61.- Incremental surface pressure distributions due to a wing fin on the cambered-twisted wing, M = 0.40, $\alpha = 8^{o}$.

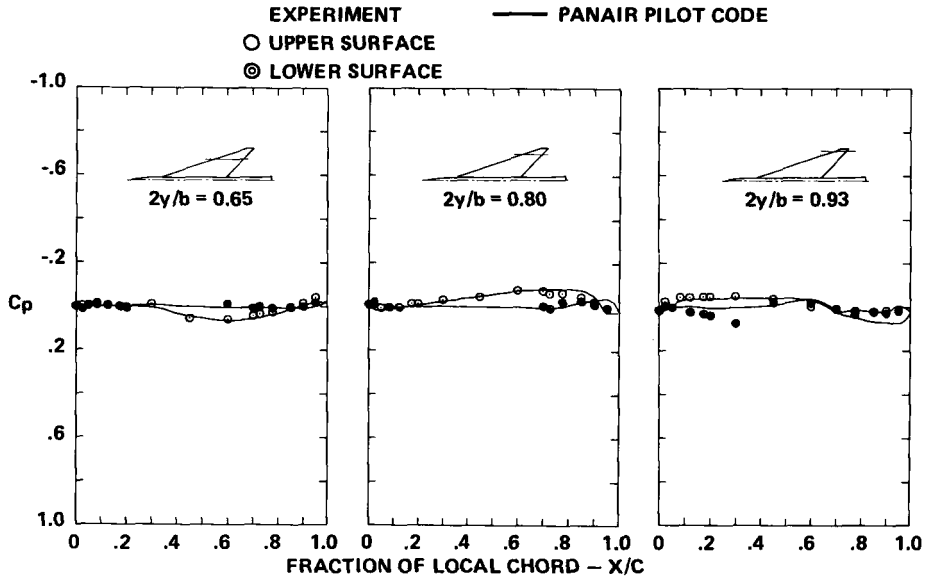

Figure 62.- Incremental surface pressure distributions due to a wing fin on the cambered-twisted wing, M = 1.05, $\alpha = 0^{o}$.

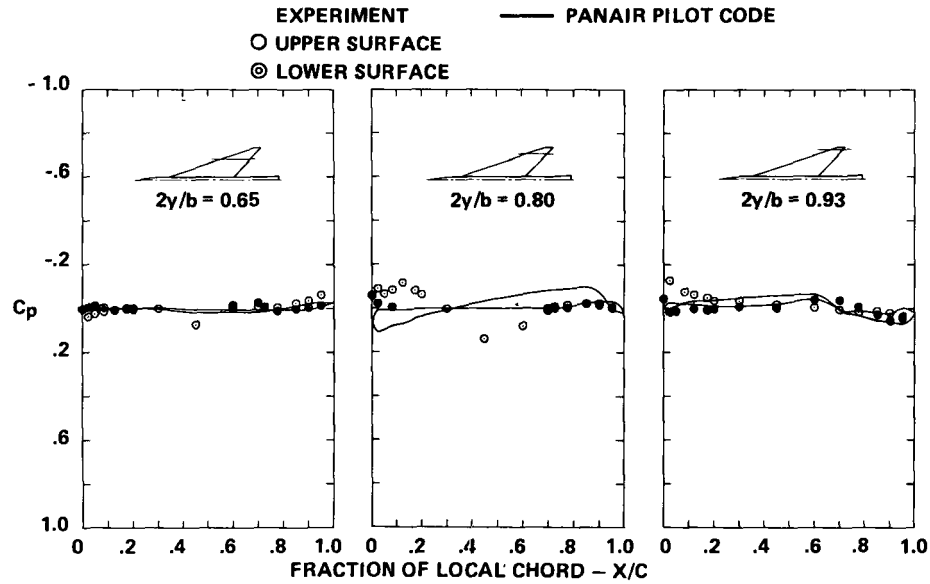

Figure 63.- Incremental surface pressure distributions due to a wing fin on the cambered-twisted wing, M = 1.05, $\alpha = 4^{o}$.

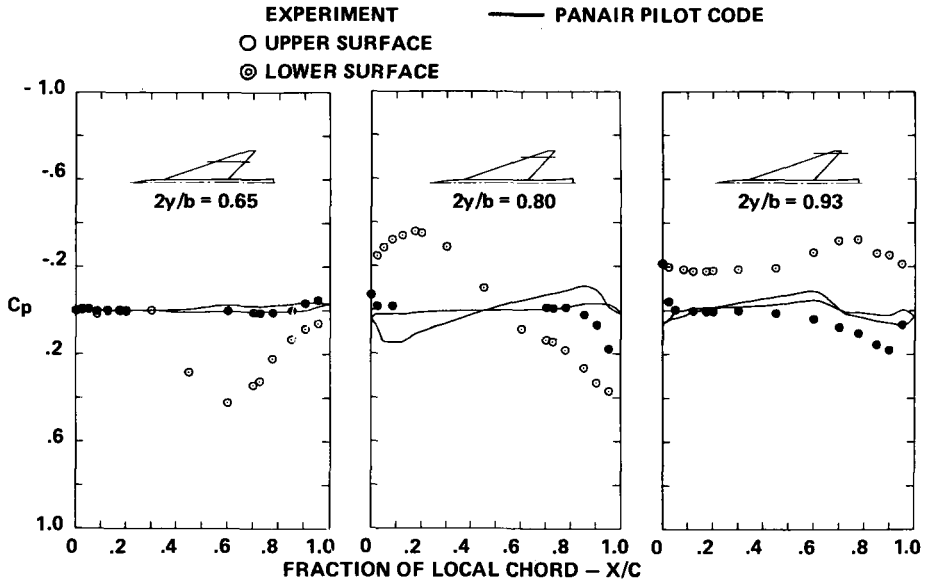

Figure 64.- Incremental surface pressure distributions due to a wing fin on the cambered-twisted wing, M = 1.05, $\alpha = 8^{o}$.

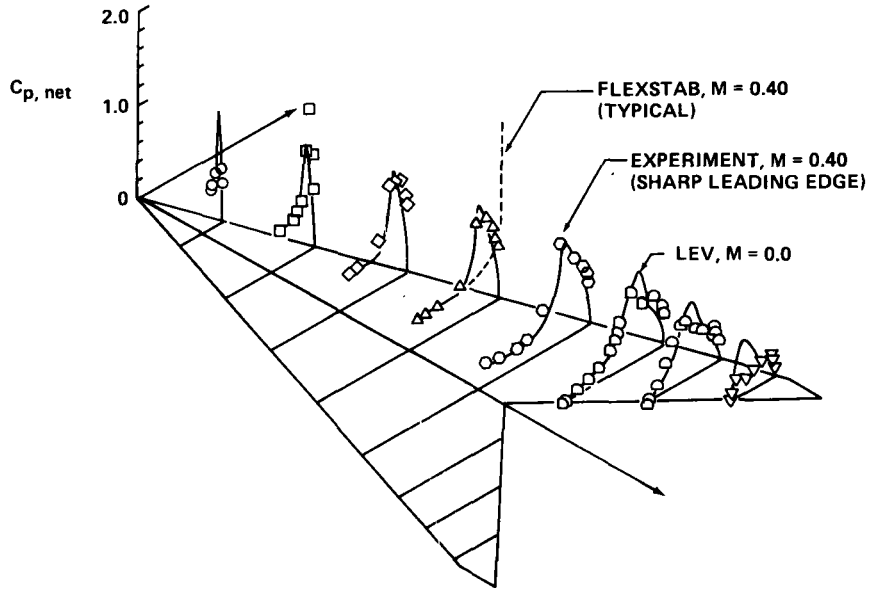

Figure 65.- Net pressure distributions, leading edge vortex (LEV) program, flat wing, $\alpha = 12^{o}$.

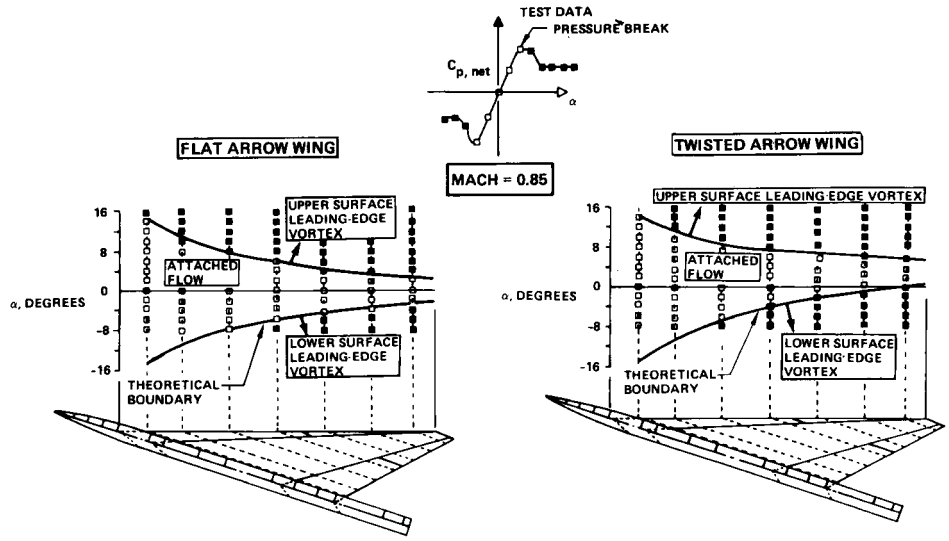

Figure 66.- Comparisons of predicted vortex development with experimental leading-edge pressures.

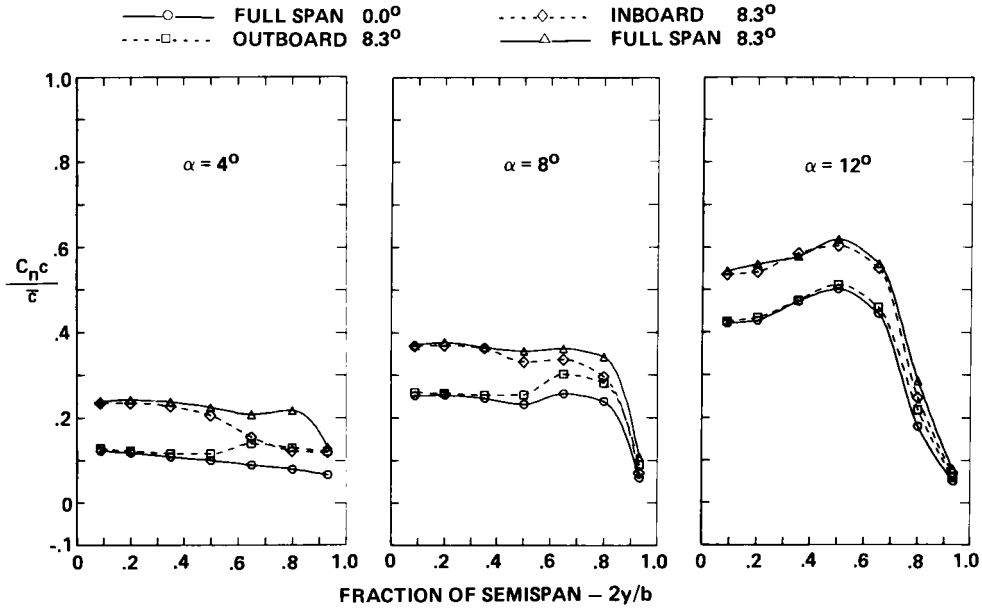

Figure 67.- Spanload distributions, effect of trailing-edge control surface deflection, flat wing, M = 0.40.

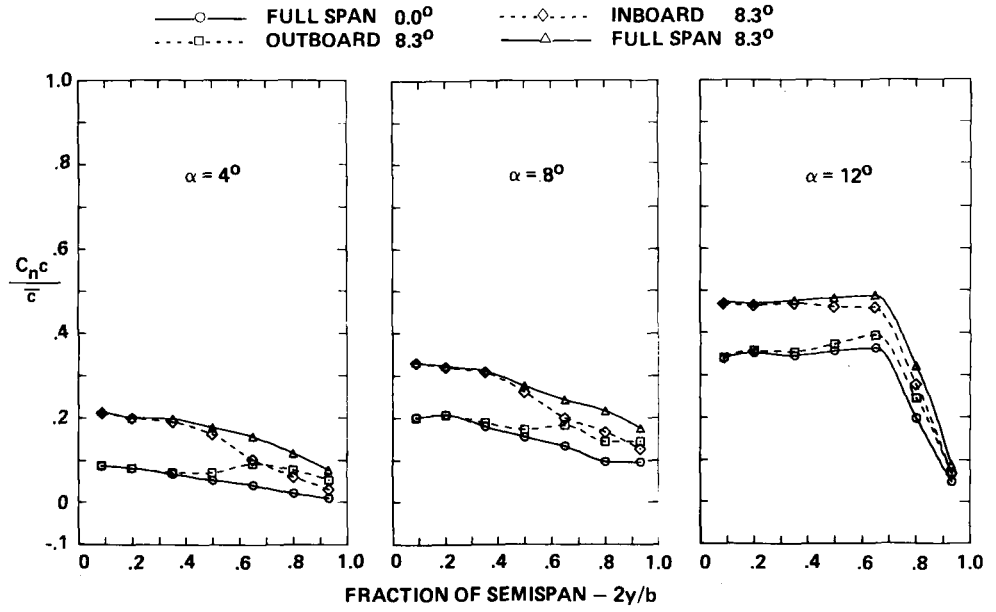

Figure 68.- Spanload distributions, effect of trailing-edge control surface deflection, twisted wing, M = 0.40.

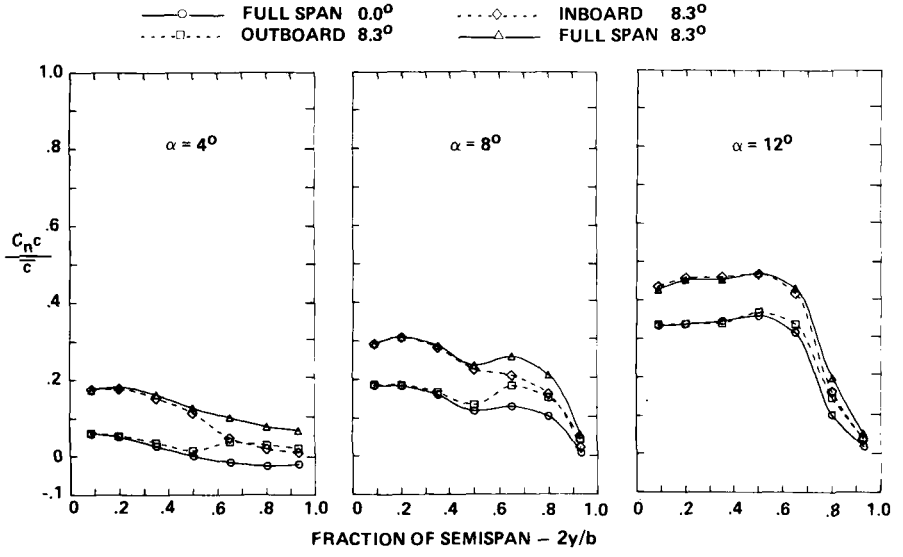

Figure 69.- Spanload distributions, effect of trailing-edge control surface deflection, cambered-twisted wing, fin off, M = 0.40.

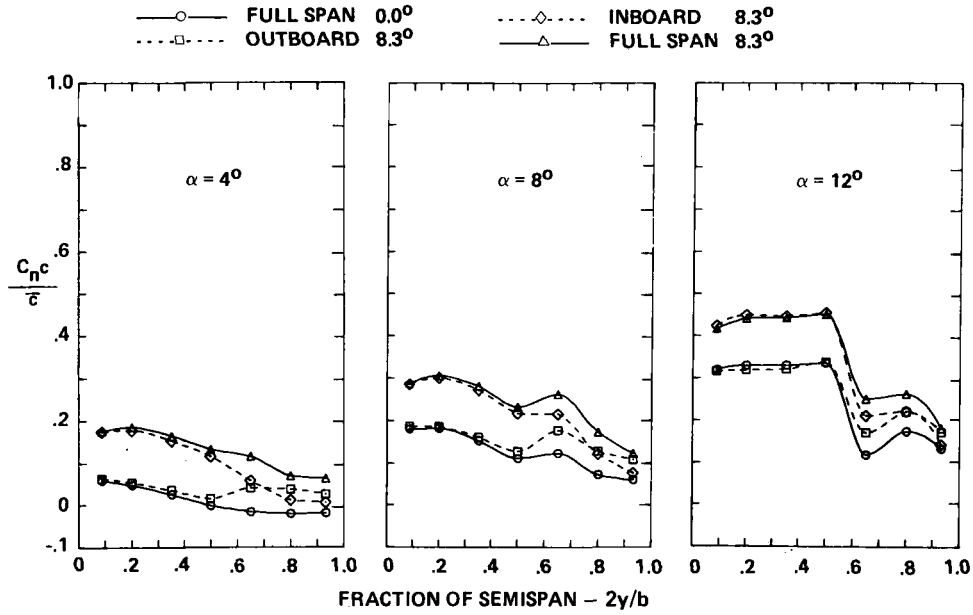

Figure 70.- Spanload distributions, effect of trailing-edge control surface deflection, cambered-twisted wing, fin on, M = 0.40.

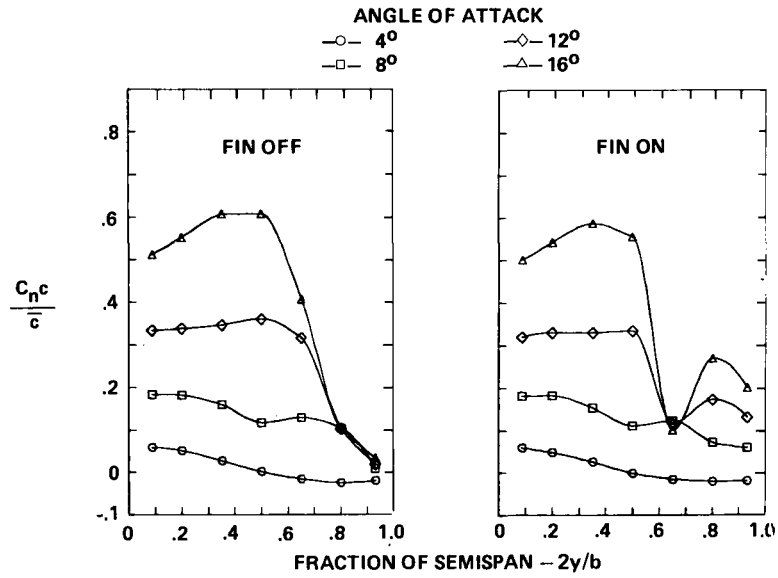

Figure 71.- Spanload distributions, effect of fin, cambered-twisted wing; T. E. deflection, full span = 0.0°; M = 0.40.

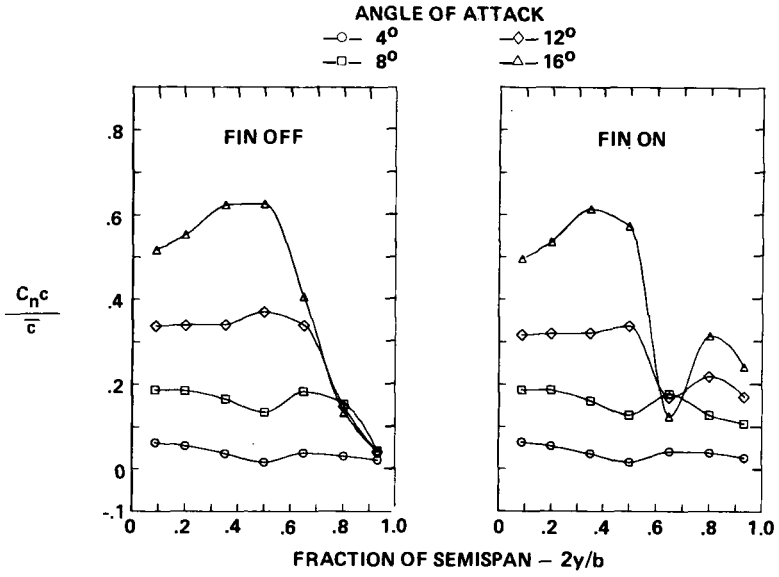

Figure 72.- Spanload distributions, effect of fin, cambered-twisted wing; T. E. deflection, inboard = 0.0°, outboard = 8.3°; M = 0.40.

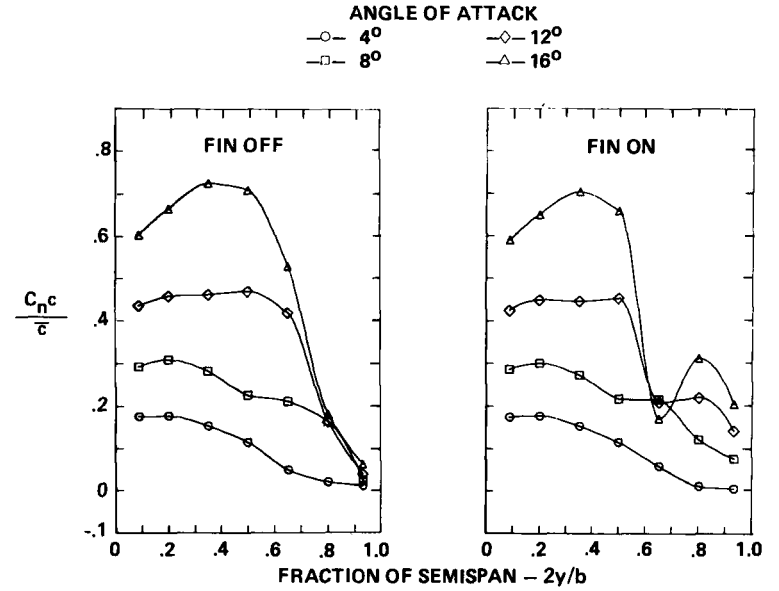

Figure 73.- Spanload distributions, effect of fin, cambered-twisted wing; T. E. deflection, inboard = 8.3°, outboard = 0.0°; M = 0.40.

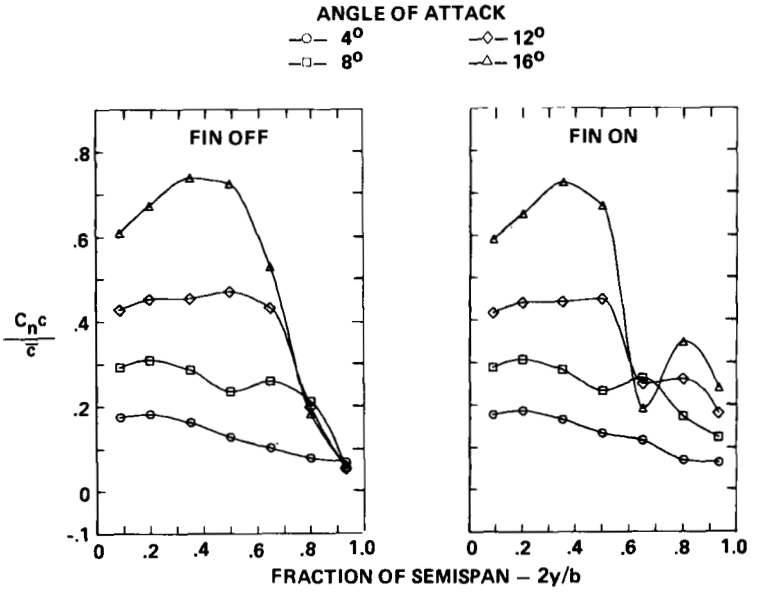

Figure 74.- Spanload distributions, effect of fin, cambered-twisted wing; T. E. deflection, full span = 8.3°; M = 0.40.